Available online at www.sciencedirect.com
ScienceDirect
Mechanics of Materials 38 (2006) 1118–1127
MECHANICS OF MATERIALS
www.elsevier.com/locate/mechmat

Modeling of residual stresses variation with thermal cycling in thermal barrier coatings

W.G. Mao [a,b], Y.C. Zhou [a,b,*], L. Yang [a,b], X.H. Yu [a,b]

[a] *Key Laboratory for Advanced Materials and Rheological Properties of Ministry of Education, Xiangtan University, Xiangtan, Hunan 411105, China*
[b] *Faculty of Materials and Optoelectronics Physics, Xiangtan University, Hunan 411105, China*

Received 27 April 2005; received in revised form 27 April 2005

Abstract

Thermal barrier coatings (TBCs) are commonly used as protective coatings for engine metal components to improve performance. Many investigations have shown that residual stresses in TBCs applications play an important role, but the residual stresses are mainly obtained by simulation method. As we know, there are a few analytical solutions of residual stress in TBCs system. In this paper, a new two-dimensional analytical solution has been obtained under the condition of non-linear coupled effects of temperature gradient, thermal fatigue, deposited residual stress, thermally grown oxide (TGO) thickening, elasto-plasticity deformation and creep deformation of TBC. Moreover, the influences of bending moment and curvature on stress variation in TBCs are considered during thermal cycling. The calculated results are in agreement with the prior experimental results.

Keywords: Thermal barrier coatings; Residual stress; Thermal cycling

1. Introduction

Thermal barrier coatings (TBCs) are commonly used as protective coatings for advanced power engineering applications to improve performance and thermal efficiency. It consists of a ceramic coating, a thermally grown oxide (TGO) that forms and thickens as the system cycles, bond coat that provides the oxidation resistance and substrate. However, thermal residual stress in TBCs accumulates in its applications due to the mismatch of material properties and high-temperature oxidation, which may directly cause adhesive failure (delamination at interface) or cohesive failure (spalling or micro-cracking within ceramic coating). Then the ceramic coating failure will result in substrate material degradation in an aggressive environment. So many researchers have realized that the evolution of residual stress plays an important role in predicting TBC failure and its durability. Elastic thermal stress in TBCs system containing graded layers has been analyzed by numerical methods (Williamson et al., 1993; Teixeira, 2001; Becker et al., 2000; Lee and Erdogan, 1994). However, the drawbacks of the

---

[*] Corresponding author. Tel.: +86 732 8293586; fax: +86 732 8292468.
E-mail address: zhouyc@xtu.edu.cn (Y.C. Zhou).

0167-6636/$ - see front matter © 2006 Elsevier Ltd. All rights reserved.
doi:10.1016/j.mechmat.2006.01.002

numerical methods lie in the fact that computations need to be performed for each change in geometrical parameters and material properties in the system.

The first analytical model for elastic thermal stresses in a bilayer system was derived by Timoshenko (1925). The analysis was based on the classical bending theory. The individual force and bending moment were assumed in each layer. There were three unknowns to be solved and three boundary conditions to be satisfied in the bilayer system. Bending moment was related to the curvature of each layer, and both layers were assumed to have the same curvature. The solution was obtained by balancing forces and moments in the system and satisfying strain continuity condition at the interface between the two layers (Timoshenko, 1925). Timoshenko's approach has been adopted by many others to analyze thermal stress in multilayer systems (Hsueh and Evans, 1985; Hsueh, 2002; Hsueh and Lee, 2003; Saul, 1969; Liu and Murarka, 1992). Hsueh and Evans had studied residual stresses in metal/ceramic bonded strips. They found that the metal may behave elastically or plastically (with full or partial plastic), depending on mechanical properties, thickness of the two constituents and thermal expansion mismatch. Residual stresses were calculated for a sequence consisting of constrained undercooling, removal of the constraint, and reheating. A general closed-form solution for elastic deformation of multilayers due to residual stress and external bending was derived by Hsueh (2002). Moreover, Hsueh and Lee had analyzed elastic thermal stress distributions in two materials joined by a graded layer (Hsueh and Lee, 2003).

However, the evolution of thermal residual stress in TBCs applications is a complicated problem due to the following factors. The deformation of material in each layer may be elastic, plastic and high-temperature creep. In particular, the TGO film forms and thickens at the ceramic coating/bond coat interface due to high temperature oxidation of the bond coat. The stress singularity in TGO near the interface has a crucial influence on the thermal residual stress distribution and interface adherence strength in TBCs. Moreover, the TGO is subject to large levels of residual compression due to its thermal expansion misfit on cooling to ambient. The compressive stress in TGO was measured by photo-stimulated luminescence piezospectroscopy (PLPS) and it could reach several GPa at ambient (Swetha et al., 2004). But the previous investigations mainly focused on the elastic thermal residual stress distribution in TBCs. The purpose of the present study is to enlarge the prior analytical model and obtain a new exact two-dimensional closed-form solution about the thermal residual stress field in TBCs under the condition of non-linear coupled effects of temperature gradient, thermal fatigue, deposited residual stress, TGO thickening, elasto-plasticity deformation and creep deformation of TBC during thermal cycling. In this model, the influences of bending moment and curvature on the variation of thermal residual stress during thermal cycling are considered and discussed.

2. Model definition

The schematic of a thermal barrier ceramic coating system is shown in Fig. 1, where the thickness of each layer is, respectively, h_c, h_t, h_b and h_s. The subscripts 'c', 't', 'b', 's' denote, respectively, the top ceramic coating, thermally grown oxide (TGO), bond coat and substrate. The coordinate system is defined so that the substrate bottom is located at $z = 0$. The system is assumed to be processed cyclic oxidation tests in air at high temperature. In addition, the system is also assumed to experience other kinds of thermal cycling tests, in which there are a large temperature gradient between the top coating and substrate. As Hsueh and Evans discussed (Hsueh and Evans, 1985; Hsueh, 2002), the stress distribution in the system is asymmetric because of the asymmetric geometry, which results in the bending of the TBCs. The distribution of strain increment in the system can be decomposed into a uniform component and bending component.

Firstly, the uniform strain increment component in TBCs will be discussed by using the following derivation logic. In the present investigation, it is

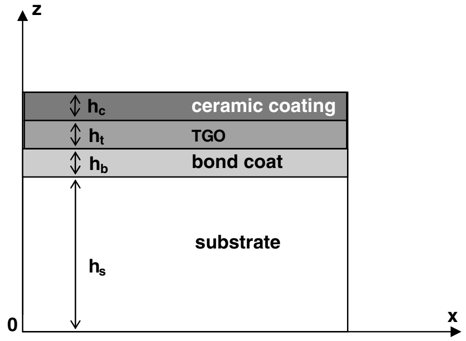

Fig. 1. A schematic of the crossing-sectional view of the TBC system.

assumed that the deformation of the ceramic coating is elastic and creep; the deformation of the bond coat, thermally grown oxide (TGO) and substrate are elasto-plasticity (Zhu and Robert, 1999; Zhou and Hashida, 2001). The stress–strain fields of each layer in TBCs are determined incrementally during the heating, holding and cooling period. They can be written as follows:

$$\mathrm{d}\varepsilon_{ij}(z,t) = \mathrm{d}e^{\mathrm{e}}_{ij}(z,t) + \delta_{ij}\,\mathrm{d}\varepsilon_m + \delta_{ij}\alpha(T)\,\mathrm{d}T(z,t) + \mathrm{d}\varepsilon^{\mathrm{c}}_{ij}(z,t) \tag{1}$$

where the $\mathrm{d}e^{\mathrm{e}}_{ij}$ represents the deviator strain increment component, δ_{ij} and $\mathrm{d}\varepsilon_m$ represent the Kronecker delta and mean strain increment, respectively. $\alpha(T)$ denotes thermal expansion coefficient. In Eq. (1), we introduce $\mathrm{d}\varepsilon^{\mathrm{c}}_{ij}(z,t)$ as creep increment of strain component in the ceramic coating. As we know, the contributions of creep deformation to thermal residual stress in constitutive equation are not considered in the prior investigations. It can be written as (Zhou and Hashida, 2001):

$$\begin{aligned}\mathrm{d}\varepsilon^{\mathrm{c}}_{ij}(z,t) &= F(t)f_1(z)A \times \exp(-Q/RT(z,t)) \times (\sqrt{3J_2}/\sigma_0)^n \times (t/t_0)^{-s}\,\mathrm{d}t \\ &= F(t)f_1(z)B(T) \times (t/t_0)^{-s}\,\mathrm{d}t\end{aligned} \tag{2}$$

where

$$B(T) = A \times \exp(-Q/RT(z,t)) \times (\sqrt{3J_2}/\sigma_0)^n \tag{3}$$

$$F(t) = \begin{cases} 1 & 0 < t < t_2 \\ 0 & t_2 < t < t_3 \end{cases} \tag{4}$$

$$f_1(z) = \begin{cases} 0 & (0 < z < h_{\mathrm{t}} + h_{\mathrm{b}} + h_{\mathrm{s}}) \\ 1 & (h_{\mathrm{t}} + h_{\mathrm{b}} + h_{\mathrm{s}} < z < h_{\mathrm{t}} + h_{\mathrm{b}} + h_{\mathrm{s}} + h_{\mathrm{c}}) \end{cases} \tag{5}$$

In the above equations, A, Q, n and s are, respectively, material constant, creep activation energy, stress exponent and time exponent. J_2 is the second invariant of the deviator stress. R, T, t denote, respectively, gas constant, temperature and time. σ_0 and t_0 are the initial stress and reference time, respectively. In Eq. (4), the physical meaning of t_i $(i = 1, 2, 3)$ denotes the different moment during the history of thermal cycling, i.e. the heating time, holding time and cooling time, respectively.

Note that material properties, such as thermal expansion coefficient $\alpha(T)$, Young's modulus $E(T)$ and Poisson's ratio $v(T)$ are dependent on temperature. For simplicity, the temperature fields in TBCs are assumed to be a linear function of the coordinate axial z (Zhou and Hashida, 2001). Therefore, the temperature fields, $T(z,t)$, can be written in the following form:

$$T(z,t) = \begin{cases} (T_1(z) - T_0) \times t/t_1 + T_0 & (0 \leqslant t \leqslant t_1) \\ T_1(z) & (t_1 \leqslant t \leqslant t_2) \\ T_1(z) - (T_1(z) - T_0) \times (t - t_2)/(t_3 - t_2) & (t_2 \leqslant t \leqslant t_3) \end{cases} \tag{6}$$

where

$$T_1(z) = \begin{cases} (T_{\mathrm{s}} - T_{\mathrm{b}}) \times z/h_{\mathrm{c}} + (T_{\mathrm{b}} - h_1 \times (T_{\mathrm{s}} - T_{\mathrm{b}})/h_{\mathrm{c}}) & (h_{\mathrm{t}} + h_{\mathrm{b}} + h_{\mathrm{s}} < z < h_{\mathrm{t}} + h_{\mathrm{b}} + h_{\mathrm{s}} + h_{\mathrm{c}}) \\ T_{\mathrm{b}} & (0 \leqslant z \leqslant h_{\mathrm{t}} + h_{\mathrm{b}} + h_{\mathrm{s}}) \end{cases} \tag{7}$$

Here T_0 and $T_1(z)$ denote, respectively, the ambient temperature and the temperature distribution in TBCs during the holding period. $T_1(z)$ is the function of position z. T_{s} and T_{b} denote, respectively, the highest temperature on the surface of the ceramic coating and that of the substrate.

The materials in TBCs are assumed to be homogeneous and isotropic. The problem is assumed to be plane stress and the stresses are regarded as equi-biaxial stress state in the following discussion, i.e. $\mathrm{d}\sigma_{11}(z,t) = \mathrm{d}\sigma_{22}(z,t) = \mathrm{d}\sigma(z,t)$ and $\mathrm{d}\sigma_{33}(z,t) = 0$. So the stress–strain increment components in TBCs can be obtained from Eq. (1):

$$\mathrm{d}\varepsilon_{33}(z,t) = -\frac{2v(T)}{E(T)}\,\mathrm{d}\sigma(z,t) + \alpha(T)\,\mathrm{d}T(z,t) + F(t)f_1(z)B(T)(t/t_0)^{-s}\,\mathrm{d}t \tag{8}$$

$$\begin{aligned}\mathrm{d}\varepsilon_{11}(z,t) &= \mathrm{d}\varepsilon_{22}(z,t) \\ &= \frac{1 - v(T)}{E(T)}\,\mathrm{d}\sigma(z,t) + \alpha(T)\,\mathrm{d}T(z,t) + F(t)f_1(z)B(T)(t/t_0)^{-s}\,\mathrm{d}t\end{aligned} \tag{9}$$

The thermal stress increment in the system can be calculated by using force balance and strain compatibility conditions. When a segment of the coating system is assumed to be constrained in the x- and y-directions, the in-plane compressive strain and stress increment will arise due to the thermal expansion on heating. The constrained thermal stress increment in the coating system can be generally derived from Eq. (9):

$$\mathrm{d}\sigma^{\mathrm{th}}(z,t) = -\frac{E(T)}{1 - v(T)} \times (f_1(z)F(t)B(T)(t/t_0)^{-s}\,\mathrm{d}t + \alpha(T)\,\mathrm{d}T(z,t)) \tag{10}$$

where $\mathrm{d}\sigma^{\mathrm{th}}(z,t)$ denotes thermal stress increment due to thermal expansion under the fully constrained condition at any given depth z. Then an equivalent tensile force increment $\mathrm{d}K$ is applied at the free boundaries and it is assumed to eliminate the restraint of the TBCs system in the x- and y-directions. So it can be obtained as follows:

$$\begin{aligned}\mathrm{d}K &= \int_0^H \mathrm{d}\sigma_{11}^{\mathrm{th}}(z,t)\,\mathrm{d}z \\ &= -\int_0^H \frac{E(T)}{1-\nu(T)} \times (B(T) f_1(z) F(t) (t/t_0)^{-s}\,\mathrm{d}t \\ &\quad + \alpha(T)\,\mathrm{d}T(z,t))\,\mathrm{d}z \end{aligned} \tag{11}$$

where H denotes the total thickness of the system, i.e. $H = h_{\mathrm{c}} + h_{\mathrm{t}} + h_{\mathrm{b}} + h_{\mathrm{s}}$. Therefore, this equivalent tensile force increment $\mathrm{d}K$ can balance the stress increment in Eq. (10) at both edges of the coating segment. Mechanical equilibrium, strain compatibility and boundary conditions can be satisfied. Then the uniform strain and stress increment resulting from the equivalent boundary force in the coating system can be obtained and written as follows, respectively,

$$\mathrm{d}\varepsilon_{\mathrm{eq}} = \frac{\int_0^H \frac{E(T)}{1-\nu(T)} \times (2f_1(z)F(t)B(T)(t/t_0)^{-s}\,\mathrm{d}t + \alpha(T)\,\mathrm{d}T(z,t))\,\mathrm{d}z}{\int_0^H \frac{E(T)}{1-\nu(T)}\,\mathrm{d}z} \tag{12}$$

$$\mathrm{d}\sigma_{\mathrm{eq}}(z,t) = \frac{E(T)}{1-\nu(T)} \times [\mathrm{d}\varepsilon_{\mathrm{eq}} - f_1(z)F(t)B(T)(t/t_0)^{-s}\,\mathrm{d}t] \tag{13}$$

If the influence of creep deformation and plasticity deformation are cancelled in Eq. (12), the simplified uniform strain increment component, $\mathrm{d}\varepsilon_{\mathrm{eq}}$, is in agreement with the results (Hsueh, 2002; Zhu and Robert, 1999) and given as follows:

$$\mathrm{d}\varepsilon_{\mathrm{eq}} = \frac{\int_0^H \left(\frac{E(T)}{1-\nu(T)} \times \alpha(T)\,\mathrm{d}T(z,t)\right)\mathrm{d}z}{\int_0^H \frac{E(T)}{1-\nu(T)}\,\mathrm{d}z} \tag{14}$$

Therefore, the thermal stress increment induced by temperature variation in the coating system can be obtained by the superposition of the stress increment due to the constrained thermal expansion in Eq. (10) and the stress increment due to the equivalent boundary force and moment in Eq. (13). It is written as follows:

$$\begin{aligned}\mathrm{d}\sigma(z,t) &= \mathrm{d}\sigma^{\mathrm{th}}(z,t) + \mathrm{d}\sigma_{\mathrm{eq}}(z,t) \\ &= \frac{E(T)}{1-\nu(T)} \times [\mathrm{d}\varepsilon_{\mathrm{eq}} - \alpha(T)\,\mathrm{d}T(z,t) \\ &\quad - 2B(T)f_1(z)F(t)(t/t_0)^{-s}\,\mathrm{d}t]\end{aligned} \tag{15}$$

Integrating Eq. (15) over time, the total stress distribution in TBCs during thermal cycling can be obtained:

$$\begin{aligned}\sigma(z,t) = C + \int_0^t \frac{E(T)}{1-\nu(T)} &\times [(\mathrm{d}\varepsilon_{\mathrm{eq}}/\mathrm{d}t) - \alpha(T) \\ &\times (\mathrm{d}T(z,t)/\mathrm{d}t) - 2f_1(z)F(t)B(T)(t/t_0)^{-s}]\,\mathrm{d}t \\ \text{for } (0 \leqslant t \leqslant t_3) \end{aligned} \tag{16}$$

where C is called integration constant, which represents initial residual stress in TBCs.

Secondly, the influence of a bending component on the stress/strain distribution in TBCs is considered, which will be determined incrementally according to each temperature increase during the heating, holding and cooling process. The bending axis is defined, as the line in the cross-section of the system where the bending strain component is zero, and the bending strain component is proportional to the distance from the bending axis and inversely proportional to the radius of curvature. Since the total stress component of each layer in TBCs during thermal cycling can be written as follows:

$$\sigma(z,t)_{\mathrm{total}} = \sigma(z,t) + \frac{E(T)}{1-\nu(T)} \times \frac{z - t_{\mathrm{b}}}{\gamma} \tag{17}$$

where $z = t_{\mathrm{b}}$ denotes the location of the bending axis and γ is the radius of curvature of the TBC system. Note that the bending axis defined by Hsueh and Evans is different from the conventional neutral axis, which has been defined in the classical beam bending theory as the line in the cross-section of the system where the normal stress is zero. As we know, the strain/stress distribution in the system is contingent upon solutions of the three parameters, $\mathrm{d}\varepsilon_{\mathrm{eq}}$, t_{b} and γ, which can be determined sequentially from the three boundary conditions (Hsueh and Evans, 1985). Moreover, the uniform strain distribution has been discussed above and obtained in Eq. (12). Then the resultant force due to the bending strain component is zero, i.e.,

$$\begin{aligned}&\int_0^{h_{\mathrm{s}}} \frac{E_{\mathrm{s}}(T)}{1-\nu_{\mathrm{s}}(T)} \times \frac{z-t_{\mathrm{b}}}{r}\,\mathrm{d}z + \int_{h_{\mathrm{s}}}^{h_{\mathrm{s}}+h_{\mathrm{b}}} \frac{E_{\mathrm{b}}(T)}{1-\nu_{\mathrm{b}}(T)} \\ &\quad \times \frac{z-t_{\mathrm{b}}}{r}\,\mathrm{d}z + \int_{h_{\mathrm{s}}+h_{\mathrm{b}}}^{h_{\mathrm{s}}+h_{\mathrm{b}}+h_{\mathrm{t}}} \frac{E_{\mathrm{t}}(T)}{1-\nu_{\mathrm{t}}(T)} \times \frac{z-t_{\mathrm{b}}}{r}\,\mathrm{d}z \\ &\quad + \int_{h_{\mathrm{s}}+h_{\mathrm{b}}+h_{\mathrm{t}}}^{H} \frac{E_{\mathrm{c}}(T)}{1-\nu_{\mathrm{c}}(T)} \times \frac{z-t_{\mathrm{b}}}{r}\,\mathrm{d}z = 0\end{aligned} \tag{18}$$

So the position of the bending axis can be determined from Eq. (18), i.e.,

$$t_b = \frac{\int_0^H \frac{E(T)}{1-v(T)} \times z\,dz}{\int_0^H \frac{E(T)}{1-v(T)}\,dz} \tag{19}$$

Finally, the sum of the bending moment with respect to the bending axis ($z = t_b$) is zero and can be obtained as follows:

$$\int_0^{h_s} (\sigma_{ts}(z,t) \times (z - t_b))\,dz + \int_{h_s}^{h_s+h_b} (\sigma_{tb}(z,t) \times (z - t_b))\,dz + \int_{h_s+h_b}^{h_s+h_b+h_t} (\sigma_{tt}(z,t) \times (z - t_b))\,dz + \int_{h_s+h_b+h_t}^{H} (\sigma_{tc}(z,t) \times (z - t_b))\,dz = 0 \tag{20}$$

where $\sigma_{ts}(z,t)$, $\sigma_{tb}(z,t)$, $\sigma_{tt}(z,t)$ and $\sigma_{tc}(z,t)$ denote, respectively, thermal stress of substrate, bond coat, TGO and ceramic coating, which can be derived from Eq. (16). The curvature, $1/\gamma$, can be determined from Eq. (20). It is written as follows:

$$\frac{1}{\gamma} = -\frac{\int_0^H \int_0^t \frac{E(T)}{1-v(T)} \times [(d\varepsilon_{eq}/dt) - \alpha(T)(dT(z,t)/dt) - 2B(T)f_1(z)F(t)(t/t_0)^{-s}]\,dt \times (z - t_b)\,dz}{\int_0^H \frac{E(T)}{1-v(T)} \times (z - t_b)^2\,dz} \tag{21}$$

where $d\varepsilon_{eq}$ and t_b are given by Eqs. (12) and (19). Similar to the Hsueh and Evans' discussion (Hsueh and Evans, 1985; Hsueh, 2002), with the solution of $d\varepsilon_{eq}$, t_b and γ, the general solutions for strain/stress distributions in TBCs have been obtained.

3. Growth of TGO

The TGO film (mainly Al_2O_3) will develop at the ceramic coating/bond coat interface in TBCs applications. But the mechanisms of alumina formation prior to Al depletion are not quantitatively comprehended, especially in the presence of TBC. Many researchers have investigated the growth law of TGO. In the reference (Evans et al., 2001), Evans et al. considered that the growth of TGO is essentially parabolic until spalling occurs:

$$h^2 = 2k_p t \tag{22}$$

where h and t represent, respectively, thickness and time. k_p is the parabolic rate constant. Itoh et al. have also obtained a growth law by fitting the experimental data (Itoh et al., 1998) and given as follows:

$$h = \lambda_0 t^{\lambda_1} \tag{23}$$

where h denotes the thickness with unit of μm and t is time with unit of s. λ_0 and λ_1 are parameters:

$$\lambda_0 = 10^{((a_0/T)+b_0)}\ \mu\text{m/s}^{-0.45} \tag{24}$$

where $a_0 = -4150$, $b_0 = 1.154$. T denotes temperature with unit of K. The parameter of λ_1 is 0.45. The details are given in Itoh et al. (1998). Therefore, the growth rate can be written as follows:

$$\frac{dh}{dt} = \lambda_0\lambda_1\left(\frac{h}{\lambda_0}\right)^{1-(1/\lambda_1)} \tag{25}$$

In the present investigation, the growth law of TGO in TBCs deduced by Itoh will be applied during the calculation. To simplify the analysis, the following assumptions are made. The oxides are assumed to form at the ceramic coating/bond coat and grow uniformly on a perfectly planar interface at the peak temperature in the cycle, with both thickening and lateral components of the growth strain, there are no shear stresses along the interface. The thermal stresses in TGO are also allowed to relax at high temperature when they attain a critical level.

4. Bond coat and TGO yield strength

In the paper, the yield strength of the bond coat and TGO are all regarded as temperature dependent. The yield characteristics of the TGO and bond coat are plotted in Fig. 2 (Karlsson and Evans, 2001). It can be seen that the TGO will yield at the peak temperature when the von Mises stress in TGO reaches ±1 GPa, imposing a maximum on the growth stress. On cooling and reheating it behaves elastically due to the rapid increase in yield strength at lower temperature (Evans et al., 2001; Karlsson and Evans, 2001). The yield strength of the bond coat is about 1000 MPa within 300 °C, and then it decreases linearly to 100 MPa as temperature increases. It is regarded as invariant when temperature is up to 850 °C. Moreover, materials characteristic in the bond coat and TGO are

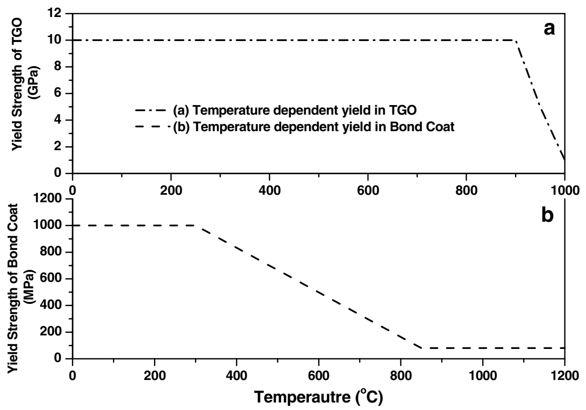

Fig. 2. The temperature-dependent yield strength of bond coat (b) and TGO (a) used for the calculation (Karlsson and Evans, 2001), as used in the prior simulations (He et al., 2002, 2003).

Table 1
Young's modulus used for the calculation

Temperature (°C)	Substrate (GPa)	Bond coat (GPa)	TGO (GPa)	TBC (GPa)
20	220	200	400	48
200	210	190	390	47
400	190	175	380	44
600	170	160	370	40
800	155	145	355	34
1000	130	120	325	26
1100	120	110	320	22

Table 2
Poisson's ratio used for the calculation

Temperature (°C)	Substrate	Bond coat	TGO	TBC
20	0.31	0.30	0.23	0.10
200	0.32	0.30	0.23	0.10
400	0.33	0.31	0.24	0.10
600	0.33	0.31	0.24	0.11
800	0.34	0.32	0.25	0.11
1000	0.35	0.33	0.25	0.12
1100	0.35	0.33	0.25	0.12

assumed to be ideal elastic–perfectly plastic materials. The von Mises yield rule is applied to judge whether the biaxial thermal residual stresses in the TGO or bond coat arrive at the temperature-dependent corresponding yield stress during thermal cycling. Moreover, material properties such as Young's modulus, Poisson's ratio and thermal expansion coefficient are temperature-dependent during the calculation and listed in Tables 1–3, respectively (Zhou and Hashida, 2001).

5. Calculation results and discussion

In order to validate the closed-form solution above, the calculated results are compared to the experimental results (Swetha et al., 2004). The system consists of a 3.2 mm thick substrate, a 75 μm grit blasted platinum-modified Ni-aluminide bond coat, a 0.5 μm thermally grown oxide (TGO) and a 150 μm 7 wt.% Y_2O_3 stabilized ZrO_2 coating. The system is assumed to be performed 1 h-cyclic oxidation tests in air at 1121 °C, which includes a 10-min heat up to 1121 °C, a 40-min hold at 1121 °C, followed by a 10-min forced-air-quench. The residual stress in the TGO has measured nondestructively by photo-stimulated luminescence piezospectroscopy (PLPS) (Swetha et al., 2004). In the present paper, a finite difference approach is used to solve Eqs. (12), (19) and (21), the temperature fields and stress–strain fields in TBCs are determined incrementally during thermal cycling.

Fig. 3 shows the evolution of compressive residual stress in the TGO after cooling to ambient during thermal cycling. The results are in agreement with the experiment data (Swetha et al., 2004). The compressive residual stress in the TGO increases quickly from the initial stress (≈1.3 GPa) in the as-received condition to approximately 2.8 GPa after 20 thermal cycles. Then it gradually decreases to 1.22 GPa after the system experiences 450 numbers of thermal cycling and approximately holds invariant in the

Table 3
Thermal expansion coefficients used for the calculation

Temperature (°C)	Substrate ($\times10^{-6}$ (°C)$^{-1}$)	Bond coat ($\times10^{-6}$ (°C)$^{-1}$)	TGO ($\times10^{-6}$ (°C)$^{-1}$)	TBC ($\times10^{-6}$ (°C)$^{-1}$)
20	14.8	13.6	8.0	9.0
200	15.2	14.2	8.2	9.2
400	15.6	14.6	8.4	9.6
600	16.2	15.2	8.7	10.1
800	16.9	16.1	9.0	10.8
1000	17.5	17.2	9.3	11.7
1100	18.0	17.6	9.6	12.2

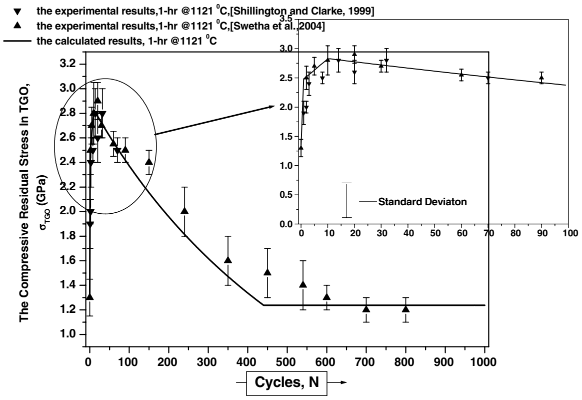

Fig. 3. Evolution of residual compressive stress in the TGO as a function of thermal cycling.

subsequent thermal cycling. The maximum standard deviation is about ±0.2 GPa in Fig. 3. Moreover, Shillington et al. have also investigated that a plasma-sprayed thermal barrier coating is observed to spall after at 1121 °C from a CoNiCrAlY bond-coated superalloy at the interface between thermally grown oxide (TGO) and zirconia thermal barrier coating (TBC) (Shillington and Clarke, 1999). They have found that the stress evolution characteristic in TGO behavior in PS TBCs has a similar manner to the stress evolution on the same bond coat under an EB-PVD coating. It is interesting that the present calculated results are also similar to their experimental results, as schematized in Fig. 3. The evolution of residual stress in TGO may result from the parabolic thickening kinetics, as discussed above. The growth of TGO thickness may slow down with thermal cycling due to the aluminum depletion in the bond coat.

The evolution of thermal residual stress in the TGO with thermal cycling is shown in Fig. 4. For the first thermal cycling, thermal stress in the TGO increases from the initial compressive stress (≈1.3 GPa) in the as-received condition to the temperature-dependent corresponding tensile yield stress during the heating period, which results in the elasto-plasticity deformation of the TGO. Then it keeps yielding state and approximately remains invariant during the holding period. On cooling, the yield stress in TGO increases quickly at lower temperatures, as has been discussed by He et al. (2002). So it is mainly regarded as elastic deformation and the compressive residual stress in the TGO is approximately 2.5 GPa due to the different coefficients of thermal expansion (CTE) and temperature variation. For the subsequent thermal cycling, the evolutions of the TGO stress change repeatedly.

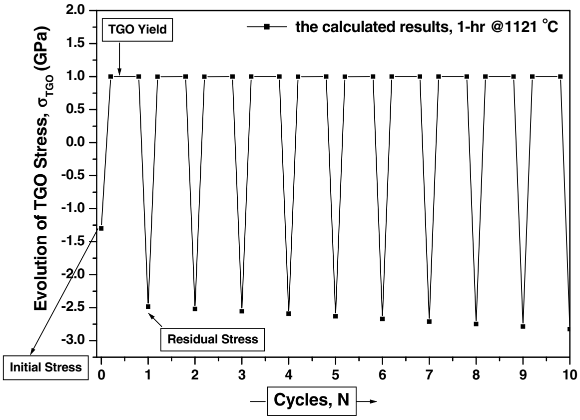

Fig. 4. Variation of the thermal residual stress in the TGO with thermal cycling. It is obvious that it keeps yielding state and approximately holds invariant (von Mises stress 1 GPa) during the holding period. On cooling to ambient, the stress state reverses again due to the CTE mismatch and temperature gradient.

Residual compressive stress in the TGO accumulates firstly with thermal cycling and then decreases gradually with respect to Al depletion in the bond coat.

In addition, the calculated results also show that the relationship between stress history in the ceramic coating and thermal cycling, as shown in Fig. 5. On heating, the stress in the ceramic coating changes from the initial compressive stress to high-temperature tensile stress. Then at high temperature during the holding period, stress-relaxation occurs in the 7 wt.% Y_2O_3 stabilized ZrO_2 coating due to the effect of creep deformation of the ceramic coating. The calculated results are consistent with the results obtained from high temperature mechanical fatigue tests (Zhu and Robert, 1999; Thurn et al.,

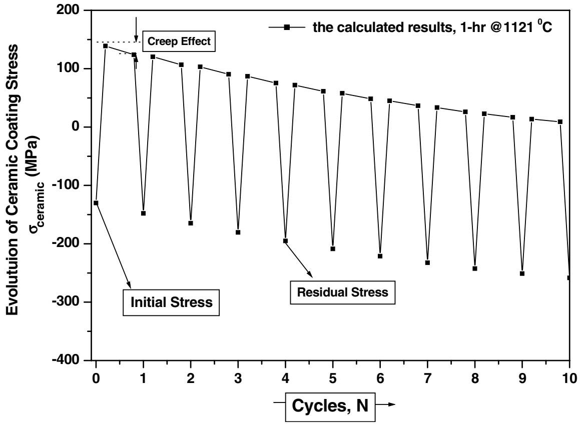

Fig. 5. The stress history in the ceramic coating vs. thermal cycling.

1997). It is important that the creep behavior of the ceramic coating in this paper also demonstrates several important issues for thermal barrier coating durability. The significant primary creep stage, as represented by time exponent, *s*, may be critical to coating life. On cooling, the material deformation in the ceramic coating can be regarded as elastic and the stress state reverses again. It is obviously seen that the accumulated residual compressive stress in the ceramic coating increases gradually with respect to thermal cycling. When an interface delamination or crack may exist at the ceramic coating/TGO interface during thermal cycling, the residual stress may develop to be large enough to induce interface crack propagation, eventually cause spalling/bucking failure of ceramic coating.

Similarly, the stress histories of the bond coat and substrate during thermal cycling are, respectively, shown in Fig. 6(a) and (b). On heating, thermal stress in the bond coat increases from the initial compressive stress to high-temperature tensile stress. During the holding period, the stress-relaxation in the substrate occurs. However, it is found that the stress evolution in the bond coat has an increase trend due to the high-temperature creep deformation of the ceramic coating. Moreover, we have found that the stress in the substrate is so small during thermal cycling that they never attain the temperature-dependent corresponding yield strength, which consists with the results discussed by Karlsson and Evans (2001) and He et al. (2000).

The evolution of residual stress distribution in TBCs with thermal cycling is shown in Fig. 7. On cooling to ambient for each thermal cycling, the residual stress in the bottom of the substrate is compressive and it is tensile at the bond coat/substrate interface. The existence of the residual stress

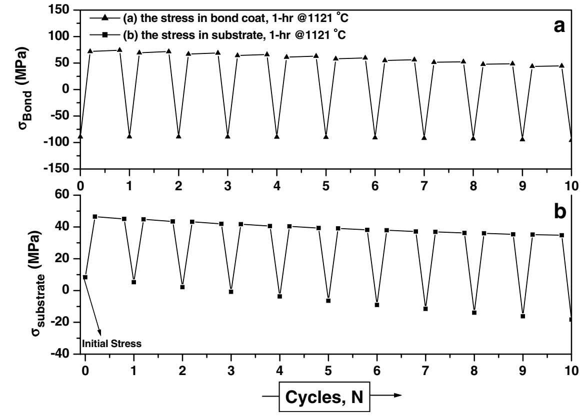

Fig. 6. (a) The stress evolution of the bond coat with thermal cycling. (b) The stress evolution of substrate with thermal cycling.

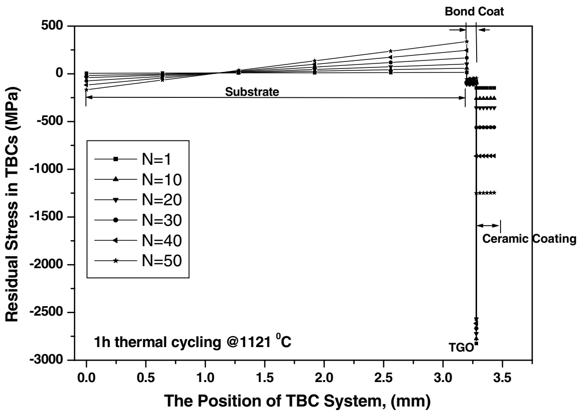

Fig. 7. The evolution of residual stress distribution of each layer in TBCs on cooling to ambient for each thermal cycling.

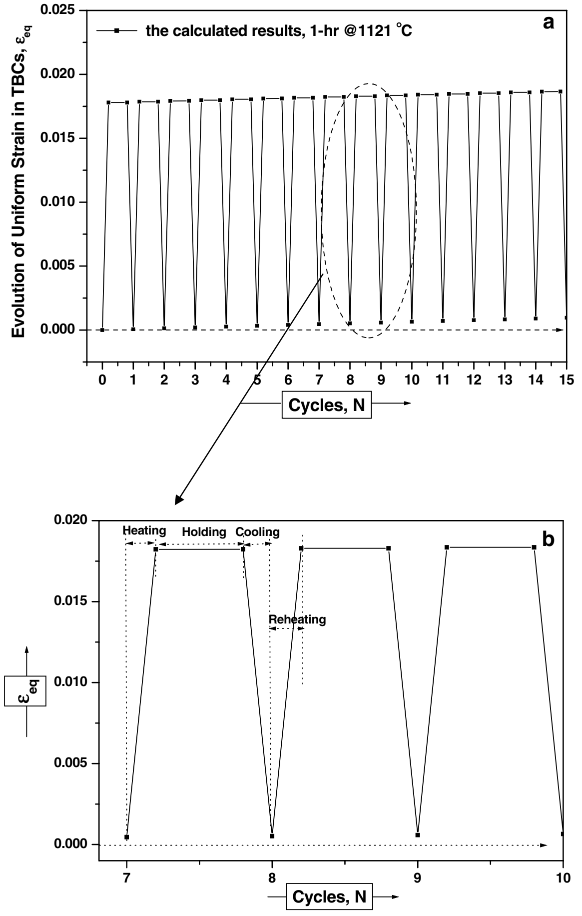

Fig. 8. (a) The evolution of the uniform strain component of the system during thermal cycling. (b) The uniform strain of the system elongates with temperature increase with thermal cycling.

characteristic in the substrate reflects the influence of bending moment of the system. The evolution of residual stress in the bond coat and ceramic coatings increases gradually with thermal cycling. But the variation of residual stress in the TGO is obviously larger than that of the other, which also reflects stress singularity located in the TGO during thermal cycling. The singularity of residual stress in the TGO will play an important role during the process of spalling/bucking failure of the ceramic coating. In order to prove the life and durability of TBCs, one should consider how to reduce the stress singularity in TBCs by optimizing graded materials, e.g., using the functionally gradient material (FGM) instead of bond coat (MCrAlY).

Variation of the corresponding uniform strain increment of the system with thermal cycling is shown in Fig. 8(a) and (b). On heating, the uniform strain of the system elongates because of temperature increase. On holding, it keeps approximately invariant. On cooling for each thermal cycling, it decreases quickly with the rapid decrease of the temperature in TBCs. It is important that the residual uniform strain exists and develops at ambient temperature due to elasto-plasticity deformation and creep deformation in TBCs during thermal cycling. It accumulates tardily with thermal cycling, as is shown in Fig. 8(b).

6. Conclusions

It is well known that the functionality and reliability of coated devices are strongly related to the variation of thermal residual stress distribution. On the basis of the prior investigations, we consider the influence of creep deformation in the ceramic coating on residual stress in constitutive equation. Finally, we have obtained a new two-dimensional analytical solution under the condition of coupled effects of temperature gradient, thermal fatigue, elasto-plasticity deformation and high-temperature creep deformation. The main conclusions of this investigation are summarized as follows.

1. The evolution rules of residual stress distributions in TBCs with respect to thermal cycling have been obtained. The variation of residual stress in the TGO is in good agreement with the prior experimental results. We found that the residual stress of TGO shown in Fig. 7 was obviously larger than that of the other layers. It is believed that the stress singularity characteristic in TGO will play an important role during the process of spalling/bucking failure of the ceramic coating.
2. It is found that the creep deformation of ceramic coating has a strong influence on thermal residual stress distribution in the ceramic coating, which mainly results in the stress relaxation in TBCs system. In addition, the stress variations in the substrate are so small that they never attain the temperature-dependent corresponding yield strength.
3. Finally, the relationship of uniform strain increment and thermal cycling had been obtained and discussed. Due to the influence of elasto-plasticity deformation and high-temperature creep deformation, the residual uniform strain of the TBCs system develops tardily with thermal cycling.

Acknowledgments

The work is supported in part by the Open Project Program of Key Laboratory of Advanced Materials and Rheological Properties, Ministry of Education, China (KF0503) and in part by Scientific Research Fund of Hunan Provincial Education Department, China under Grant 05C096.

References

Becker, T.L., Cannon, B.M., Ritchie, R.O., 2000. An approximate method for residual stress calculation in functional graded materials. Mech. Mater. 32, 85–97.

Evans, A.G., Mumm, D.R., Hutchinson, J.W., 2001. Mechanisms controlling the durability of thermal barrier coatings. Progr. Mater. Sci. 46, 505–553.

He, M.Y., Evans, A.G., Hutchinson, J.W., 2000. The ratcheting of compressed thermally grown thin films on ductile substrates. Acta Mater. 48 (10), 2593–2601.

He, M.Y., Hutchinson, J.W., Evans, A.G., 2002. Large deformation simulations of cyclic displacement instabilities in thermal barrier systems. Acta Mater. 50, 1063–1073.

He, M.Y., Hutchinson, J.W., Evans, A.G., 2003. Simulation of stresses and delamination in a plasma-sprayed thermal barrier system upon thermal cycling. Mater. Sci. Eng. A 345, 172–178.

Hsueh, C.H., 2002. Modeling of elastic deformation of multilayers due to residual stresses and external bending. J. Appl. Phys. 91 (12), 9652–9656.

Hsueh, C.H., Evans, A.G., 1985. Residual stresses in metal/ceramic bonded strips. J. Am. Ceram. Soc. 68 (5), 241–248.

Hsueh, C.H., Lee, S., 2003. Modeling of elastic thermal stresses in two materials joined by a graded layer. Composites, Part B 34, 747–752.

Itoh, Y. et al., 1998. Basic study of oxidation behavior of zirconia thermal barrier coating at high-temperature. J. Sco. Mater. Sci. Jpn. 47 (7), 665–671.

Karlsson, A.M., Evans, A.G., 2001. A numerical model for the cyclic instability of thermally grown oxides in thermal barrier systems. Acta Mater. 49 (10), 1793–1804.

Lee, Y.D., Erdogan, F., 1994. Residual/thermal stresses in FGM and laminated thermal barrier coatings. Int. J. Fract. 69 (2), 145–165.

Liu, H.C., Murarka, S.P., 1992. Elastic and viscoelastic analysis of stress in thin films. J. Appl. Phys. 72 (8), 3458–3463.

Saul, R.H., 1969. Effect of GaAsxP12x transition zone on the perfection of GaP crystals grown by deposition onto GaAs substrates. J. Appl. Phys. 40 (8), 3273–3279.

Shillington, E.A., Clarke, D.R., 1999. Spalling failure of a thermal barrier coating associated with aluminum depletion in the bond-coat. Acta Mater. 47 (4), 1297–1305.

Swetha, S., Xie, L.D., Jordan, E.H., et al., 2004. Stress variation with thermal cycling in the thermally grown oxide of an EB-PVD thermal barrier coating. Surf. Coat. Technol. 179, 286–296.

Teixeira, V., 2001. Numerical analysis of the influence of coating porosity and substrate elastic properties on the residual stresses in high temperature graded coating. Surf. Coat. Technol. 146/147, 79–84.

Thurn, G., Schneider, G.A., Aldinger, F., 1997. High-temperature deformation of plasma-sprayed ZrO_2 thermal barrier coatings. Mater. Sci. Eng. A 233, 176–182.

Timoshenko, S., 1925. Analysis of bi-metal thermostats. J. Opt. Soc. 11, 233–255.

Williamson, R.L., Rabin, B.H., Drake, J.T., 1993. Finite element analysis of thermal residual stresses at graded ceramic-metal interfaces. Part I. Model description and geometrical effects. J. Appl. Phys. 74 (2), 1310–1320.

Zhou, Y.C., Hashida, T., 2001. Coupled effects of temperature gradient and oxidation on thermal stress in thermal barrier coating system. Int. J. Solids Struct. 38, 4235–4264.

Zhu, D.M., Robert, A.M., 1999. Determination of creep behavior of thermal barrier coatings under laser imposed high thermal and stress gradient conditions. J. Mater. Res. 14 (1), 146–161.

Available online at www.sciencedirect.com
ScienceDirect
Surface & Coatings Technology 201 (2007) 6217–6227
SURFACE & COATINGS TECHNOLOGY
www.elsevier.com/locate/surfcoat

An experimental investigation on thermo-mechanical buckling delamination failure characteristic of air plasma sprayed thermal barrier coatings

W.G. Mao [a,b], C.Y. Dai [a,b], Y.C. Zhou [a,b,*], Q.X. Liu [a,b]

[a] Faculty of Materials and Optoelectronics Physics, Xiangtan University, Hunan, 411105, China
[b] Key Laboratory of Low Dimensional Materials and Application Technology, Ministry of Education, Xiangtan University, Hunan, 411105, China

Received 10 June 2006; accepted in revised form 14 November 2006
Available online 17 January 2007

Abstract

The primary intention of this work is to investigate the thermo-mechanical buckling delamination failure characteristic of air plasma sprayed thermal barrier coatings (TBCs) under compression tests at high temperature. The TBCs samples with a pre-delamination were firstly designed and they had been successfully prepared by air plasma sprayed technique. The main novelty of this paper is that the first work to validate and obtain three kinds of the interface failure forms in TBCs system during compression tests, i.e. buckling delamination, edge delamination and global buckling failure. The effects of the initial delamination length, temperature gradient and applied mechanical load on the delamination resistance of the TBCs system were discussed in detail. It is difficult to observe buckling delamination or edge delamination failure phenomena until the initial delamination length in TBCs reaches or exceeds 4 mm or more. For edge delamination failure, the interface fracture toughness (Γ_i^{II}), energy release rate (G_{ss}^{edge}) and stress intensity factor (K_{II}) between the TBC/TGO interface were 35 J m^{-2}, 38.8 J m^{-2} and 0.97 MPa $\sqrt{m}$ at high temperature gradient, respectively. Using scanning electron microscopy (SEM) and energy dispersive X-ray (EDX), it was inferred that the delamination fracture located within the ceramic coating close to the TBC/TGO interface. The results agree well with other experimental and theoretical results.

Keywords: Thermal barrier coatings; Buckling delamination; Edge delamination; Thermal gradient

1. Introduction

Thermal barrier coating (TBC) is commonly used as protective coatings for advanced power engineering devices to improve performance and thermal efficiency [1]. It consists of a top ceramic coating (TC), a thermally grown oxide (TGO) that forms and thickens as the system cycles, bond coat (BC) that provides the oxidation resistance and substrate. The great difference in the thermo-mechanical properties of metals and ceramics seems to preclude their applications in composite structures subjected to huge changes in temperature and thermal stresses. Various failure modes have been observed, but one of the most common ones is cracking at the TC/TGO or TGO/BC interface leading to buckling delamination and spalling [2–4], which may result in the associated problems of structural integrity and stability, reduction in load-bearing capacity, stiffness degradation and fracture of TBCs.

Most delamination buckling failures related to TBC investigations have primarily focused on the formulation of analytical solutions for the prediction of the buckling behaviour [3,5–8]. Hutchinson et al. have analyzed the influence of prototypical imperfections on the nucleation and propagation stages of delamination of compressed thin films [5]. Energy release rates for separations that developed from imperfections have been calculated. A critical film thickness for nucleation and a critical imperfection wavelength for buckling has been obtained and discussed in detail. Patterson et al. have studied the delamination buckling and spalling of plasma-sprayed thermal barrier coatings by using basic concepts from fracture mechanics and the theory of crack propagation. An upper bound for the maximal allowable thickness of a coating was derived which took into account the fracture toughness of the coating as well as the mismatch in both thermal and mechanical properties

---

[*] Corresponding author. Faculty of Materials and Optoelectronics Physics, Xiangtan University, Hunan, 411105, China. Tel.: +86 732 8293586; fax: +86 732 8292468.
E-mail address: zhouyc@xtu.edu.cn (Y.C. Zhou).

0257-8972/$ - see front matter © 2006 Elsevier B.V. All rights reserved.
doi:10.1016/j.surfcoat.2006.11.025

of the coating and substrate [6]. Among the few previous experiments, Gell et al. have studied the durability and failure mechanisms of solution precursor plasma spray (SPPS) TBCs [9]. The SPPS TBCs exhibited an average life of 1018 cycles in a 1-h 1121 °C cycle furnace test. It is found that the failure of the SPPS TBCs started with crack initiation along the unmelted particles in the ceramic top coat and the non-alumina oxides. When a crack of sufficient size emerged, the TBC separated from the metal substrate by large scale buckling. Shaw et al. [10] have designed a chevron-notched sandwich specimen for the first time, and then measured the interface fracture energy of air plasma sprayed 8-wt.% yttria stabilized zirconia (YSZ) thermal barrier coatings for both the as-received and thermal cycled specimens. It is found that the thermal cycles slightly reduced the toughness of the TBCs and caused the failure location to shift from within the YSZ about 100-μm away from the interface to the near-interface region. But Thurn et al. [11] have performed the atmospheric plasma-sprayed zirconia removed from the substrate by three-point micro-bending test equipment. It is found that the critical energy release rate of the through-thickness cracks did increase with annealing temperature while the work of fracture of delamination cracks decreased. Brodin et al. investigated the influence of oxidation on mechanical and fracture behaviour of an air plasma-sprayed NiCoCrAlY bond coat by bending test at ambient condition. Their results indicated that the crack propagation resistance increased with oxidation, which probably was a result of an increased oxide network, local deformation and less brittle grain-boundaries [12].

As we know, at present there are few experimental methods to investigate the buckling delamination characteristics of plasma sprayed TBCs at high temperature. It is difficult to forecast and obtain the buckling failure phenomena of TBCs by controlling the experimental conditions. In this paper, a testing method is introduced to successfully fabricate the delaminated TBCs samples. This paper mainly focuses on the experimental study of buckling delamination failure in delaminated TBCs system by compression tests at high temperature, duplicating the service failure mode. This investigation would be beneficial to recognize the buckling failure behaviour of the ceramic coating and provide the useful experimental data.

2. Experimental

2.1. Delaminated TBCs specimen preparation

The material properties of each layer of the TBC sample are listed in Table 1. The SUS304 stainless steel samples were used as substrates for the present study in the form of beams of $40 \times 5 \times 5$ mm^3. It is rather difficult to predict and evaluate the delamination buckling location, its propagation path and critical load due to a number of complicated factors such as the coating stresses, thickness, interface adhesion strength and high temperature gradient. It is necessary to design and make pre-patterned regions of low adhesion (i.e. pre-delaminated interface region) at the TBC/Substrate interface to constrain the delamination buckling path, which can provide more predictable behaviour. The experimental procedure for patterning regions of low adhesion surrounded by regions of higher adhesion for the ceramic coating on NiCrAlY bond coat is briefly addressed in Fig. 1. All the preparation process included five steps. In step 1, the samples were ground and polished to 7 μm before grit blasting. The preparation techniques utilized dry blasting by corundum powder with 60 mesh grain size distribution. The subsequent step to the abrasive treatment was preheating in order to remove contaminants such as moisture and volatiles. After this procedure, the substrates were coated with NiCrAlY powder (grain size distribution 20–50) applied by low pressure plasma spray. The distance between the plasma torch and the substrate was held constant at 70 mm, for both bond coat and the following ceramic coating. The thickness of the BC is about 100 μm. The next step was the thermal treatment at high temperature in vacuum (~1000 °C/2 h) in order to diffuse the coated layer and the substrate. The bond coat was also grit blasted prior to TBC deposition by plasma sprayed process. In step 2, the surface of bond coat was tightly wrapped by a soft steel slice except that the desired low adhesion pattern region was exposed, waiting for spraying Al_2O_3 powder with size distribution of 60±μm. The exposed area (or the area of the low adhesion region) was easily controlled. And then the Al_2O_3 powder was sprayed on the surface in step 3. The thickness of the Al_2O_3 layer was approximately controlled within the range 3 μm and used to create the low adhesion regions. It is clear that this layer is absent in the other regions of higher adhesion. After this, the covered soft steel slice was carefully removed from the bond coat and the small region of the Al_2O_3 layer was left at the desired low adhesion region, as shown in step 4. Note that the thickness and length of the Al_2O_3 layer were approximately

Table 1
Specification of the samples for thermal cycling test and high temperature compression testing

Layer	Composition (%)	Process	Thickness
Top coat	8 wt.% Y_2O_3–ZrO_2	APS	~300 μm
Bond coat	NiCrAlY	APS	~100 μm
Substrate	SUS304 stainless steel	Investment casting	~5 μm

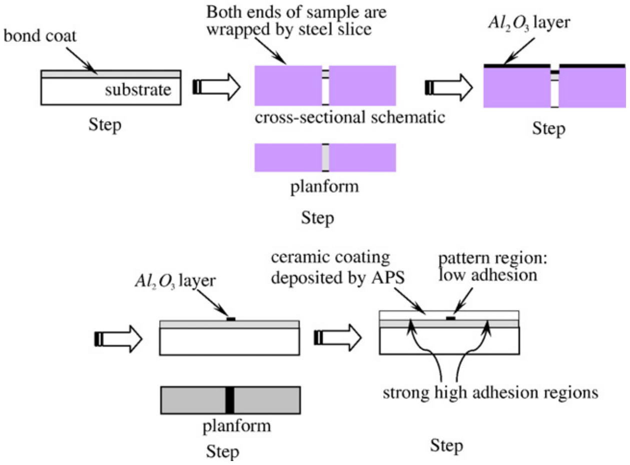

Fig. 1. The schematic drawing for creating interface patterns of low adhesion.

Table 2
Specification of the delaminated TBCs samples

TBCs sample number	A	B	C	D	E
Delamination length, i.e. the length of low adhesion region (denoted L)	1 mm	2 mm	5 mm	8 mm	10 mm
The thickness of Al_2O_3 layer	3 μm	3 μm	3 μm	3 μm	3 μm

regarded as the thickness and length of low adhesion regions (i.e. initial interface delamination, denoted A–E, see Table 2). The final step was that the 8 wt.% Y_2O_3–ZrO_2 powder with size distribution of 20±10 μm was sprayed as a top coating after the covered soft steel slice was carefully removed from the bond coat. The substrate temperature was approximately 200 °C. The distance between target and substrate was about 60 mm. The detailed plasma-spray conditions can be found elsewhere [13]. In this paper, the residual Al_2O_3 layer at the central interface between the TC and BC layers represents the low adhesion regions. Although no direct observation of the location of the interface delamination has been made by scanning electron microscopy (SEM), it is believed that the separation occurs either within the Al_2O_3 layer or at the TC/Al_2O_3 interface. The validity and feasibility of this test design method will be proved by the following thermo-mechanical compressive test. In fact, a similar design method has been proved and applied to study the buckling failure behaviour in other film/coating system [14].

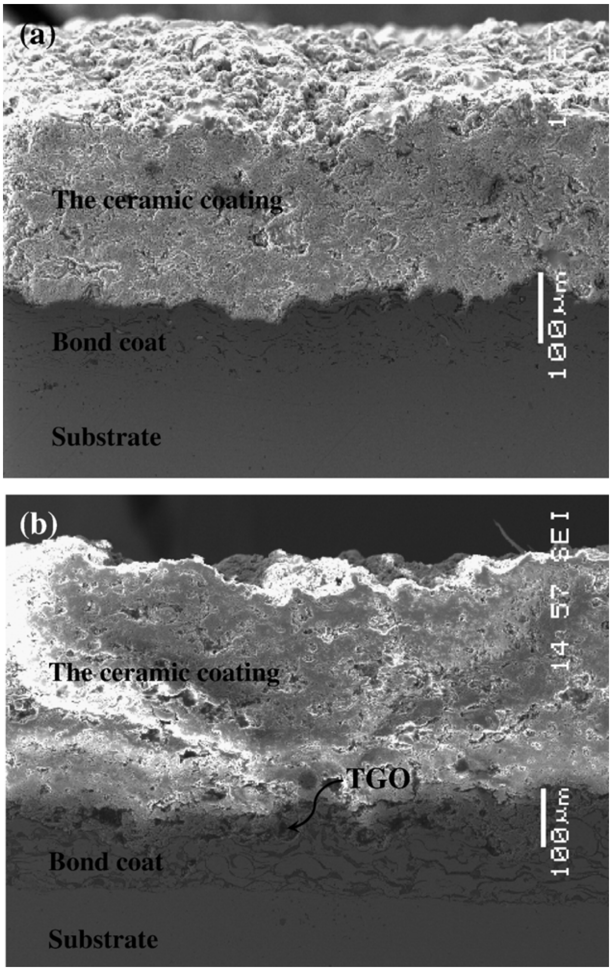

Fig. 2. The SEM micrographs of the cross-section near the low adhesion regions, (a) the as-received TBC and (b) the heat treated TBC (200 h).

2.2. Experimental method and microstructure

To accord with the practical application of TBCs, thermal cycling tests were performed by high temperature furnace. The thermal cycle consisted of a 10-min heat-up from room temperature to 1000 °C, a 100-min holding at 1000 °C and a 10-min forced air quench. The total thermal aging time is approximately 200 h. The microstructures of the cross-section morphology for both the as-received and heat treated TBCs samples are shown in Fig. 2(a) and (b). Fig. 2(a) shows the typical microstructure of as-processed coatings, in which large amounts of microcracks and pores are characterized in conjunction with a platelet (or splat) structure. A thin thermally grown oxide (TGO) film formed and thickened with thermal cycling (See Fig. 2(b)). But no distinct delamination or microcracks was observed at the TBC/TGO interface. And then the samples would be carried out the compressive tests (equipment model: REGER 2000-10) were carried out at high temperature.

The thermo-mechanical compressive experiment setup in this work is shown in Fig. 3. The delaminated TBCs samples can be heated up to 1200 °C or more by oxyacetylene torch heating equipment. Three pieces of thermocouples were used to measure, respectively, the top surface temperature of the ceramic coating (denoted T_1), the bottom surface temperature of the substrate (denoted T_2) and the cross-section temperature of the TBCs sample (denoted T_3). A total of 50 samples were tested. Each test was firstly loaded to 2000 N with a rate of about 100 N/min by load control mode. And then the compressive load remained invariable for an hour. The TC surface was heated to high temperature by oxyacetylene torch setup until the buckling failure phenomena of the TC occurred. Note that the flame of the torch only heated the surface of the TC rather than the other surfaces, as shown in Fig. 3. The

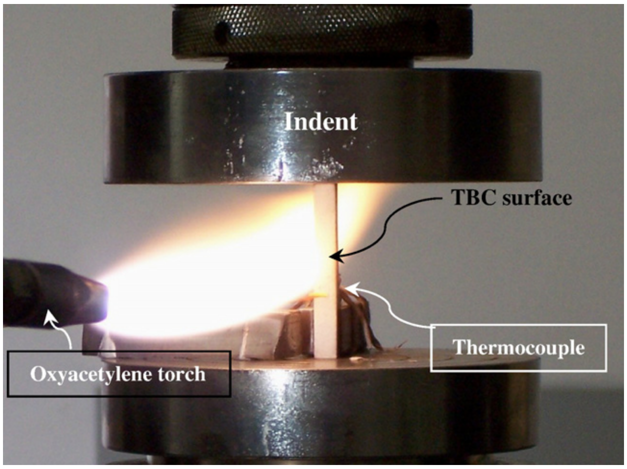

Fig. 3. The thermo-mechanical compression test equipment, the oxyacetylene torch heating equipment and thermocouple measurement setup. The white background is the lab's wall.

oxyacetylene torch, whose axis was orthogonal to the TC surface, was translated at a constant velocity of 2 cm/s so that the surface of the TC could be heated uniformly. Furthermore, the maximum temperature of the TBC surface was easily controlled within the range of 1000–1300 °C by adjusting the distance between the torch flame and the TBC surface. The corresponding critical temperature magnitude and mechanical load were recorded for each test and could be utilized to calculate the interface toughness or stress intensity factor. All samples were unloaded once the visible delamination buckling failure of the ceramic coating occurred.

It should be noted that a problem associated with flat-plate compression test specimens was the possibility of material global failure (e.g. substrate buckling failure) rather than the desired delamination buckling of the ceramic coating under compressive loads (denoted ΔT) and high temperature gradient (denoted P). This problem was eliminated by selecting the compressive load whose magnitude was much lower than the ultimate critical buckling load of the substrate material. The fracture location of the ceramic coating was determined and analysed by HITACHI S-570 scanning electron microscopy (SEM) and energy dispersive X-ray (EDX).

2.3. Fracture toughness studies

For a film/coating in compression, the interface crack is in mode II, so the faces remain in contact behind the advancing tip [15]. Hutchinson has recongized that under the idealized assumption that frictional sliding plays a negligible role. The steady-state energy release rate of the crack is given by the equation: i.e. $G = G_0$, when its length is several times the coating thickness. Thus, if the mode II toughness of the interface is Γ_i^{II} (measured in units of energy per unit area), then the critical combination of the coating stress and thickness at which the edge-delamination can spread without arrest is [5]:

$$\sigma_0 = \sqrt{\frac{2E\Gamma_i^{II}}{(1-v^2)h}} \tag{1}$$

where σ_0 represents the stress in the ceramic coating. E, v and h denote the Young's modulus, Poisson's ratio and thickness of the ceramic coating, respectively. The mode II toughness of the interface, Γ_i^{II}, can be evaluated when σ_0 in the TC is given. When a delamination crack emerges from an edge along the interface, the force and moment are released, giving rise to an energy release rate which approaches from below the steady-state energy release rate [15]:

$$G_{ss}^{edge} \equiv \frac{\bar{\sigma}^2 h}{2\ \bar{E}_{\mathrm{tbc}}} + \frac{\Delta\sigma^2 h}{24\ \bar{E}_{\mathrm{tbc}}} \tag{2}$$

where $\bar{\sigma}$ denotes the average stress in the TBC. $\Delta\sigma$ represents the stress difference between the top surface and the interface. A prototypical steady-state temperature distribution for a thermal barrier system is used to relate G_{ss}^{edge} to the thermal environment, with T_{dep} being the stress-free temperature, T_0 the temperature at the TBC surface, T_i the temperature at the interface with the bond coat and T_{cool} the alloy temperature at the cooling channels [16]. So the substrate temperature is taken as $\bar{T} = (T_0 + T_{\mathrm{cool}})/2$. In this work, the values of these temperatures are measured by thermocouples, as shown in Fig. 3. Under the combined influence of thermal gradient and those generated by the application of an external mechanical load, the $\bar{\sigma}$ and $\Delta\sigma$ are obtained as follows,

$$\Delta\sigma = \bar{E}_{\mathrm{tbc}}\alpha_{\mathrm{tbc}}(T_i - T_0) \tag{3}$$

$$\bar{\sigma} = \overline{2}E_{\mathrm{tbc}}\left\{\alpha_s(\bar{T} - T_{\mathrm{dep}}) - \alpha_{\mathrm{tbc}}[(T_0 + T_i)/2 - T_{\mathrm{dep}}]\right\} + P/S \tag{4}$$

This critical energy release rate is subject to strictly mode II (shear) loading, since $\bar{\sigma}$ is a compression force [15]. In Eq. (4), the first term represents thermal stress induced by temperature change. The second term denotes mechanical stress induced by external compressive load. P is compressive load at both edges. S denotes the cross-sectional area of the TBCs system. As we know, T_{dep} is in the range 700–1100 °C, and T_0 is above 1100 °C, the energy release is dominated by the $\bar{\sigma}$ term in Eq. (2), which in turn is predominantly governed by the Eq. (4), since the substrate temperature under the operational conditions is near the deposition temperature. In other words, the dominant stress contribution is due to the elevation of the average temperature in the ceramic coating above the deposition temperature [16]. So the effective energy release rate becomes:

$$G_{ss}^{\mathrm{edge}} \approx \frac{h}{2\bar{E}_{\mathrm{tbc}}}\left(\frac{P}{S} - \bar{E}_{\mathrm{tbc}}\alpha_{\mathrm{tbc}}[(T_0 + T_i) - 2T_{\mathrm{dep}}]\right)^2 \tag{5}$$

3. Results and discussion

In the previous studies, the spallation location for electron beam physical vapour deposition (EB-PVD) TBCs is normally at the interface between the thermally grown Al_2O_3 and the bond coat, whereas it is typically located within the zirconia ceramic just above the Al_2O_3 layer in plasma sprayed coatings [17–21]. In this work, it was also found that the failure location initiated as an interface delamination which rapidly propagated by thermo-mechanical loads. When the delamination crack became large enough, either large scale buckling or edge delamination were activated. Buckling delamination and edge delamination failure of the ceramic coating were observed when the initial interface delamination of TBCs became larger than 4 mm or more. Both will be discussed in the following, respectively.

3.1. Typical buckling delamination failure mode

Fig. 4 showed that the buckling delamination of the ceramic coating occurred when $P = 2kN$, $L = 10$ mm, $T_1 = 1370$ °C and $T_2 = 985$ °C. The length and deflection of buckling failure region of the ceramic coating were, respectively, about 14 mm and 1.5 mm. Hutchinson et al. have found that the critical interface delamination length (denoted L_b) is about 20 h (h is the thickness of the coating) or more for typical moduli and film/coating compression levels [5]. The experimental results were in agreement with their theoretical results. Fig. 4(b) and (c)

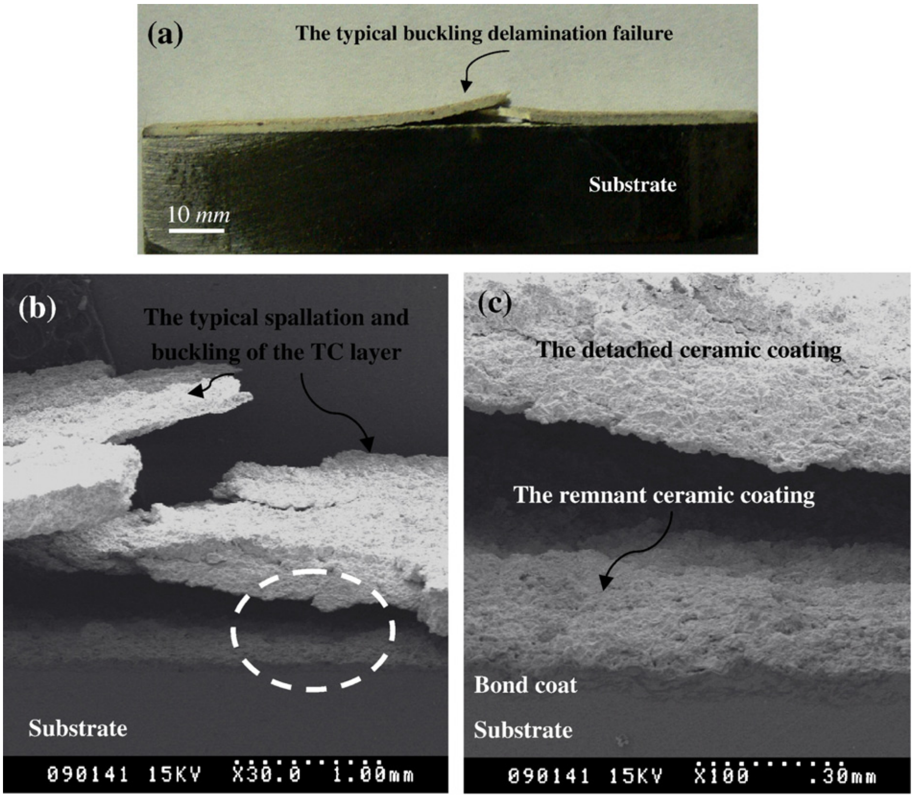

Fig. 4. The images of the typical buckling delamination failure after thermo-mechanical compression test, where $L = 10$ mm. (a) the digital camera photograph. (b) the SEM image of the cross-sectional microstructure at the central region of the sample. The buckling delamination failure morphology can be more clearly observed. Fig. (c) is magnified from the dashed round region of Fig. (b). A thin ceramic coating adheres to the bond coat, which also proves that the fracture location lies within the TBC just above the low adhesion region.

represented the polished cross-sectional microstructures of the delaminated samples (in Fig. 4(a)). The typical spallation and buckling rupture of the TC layer were observed after thermo-mechanical compressive test. Fig. 4(c) was magnified from the dashed round region of Fig. 4(b). It was clearly seen that a thin ceramic coating adhered to the bond coat, which substantially proved that the fracture location lay within the ceramic coating. The EDX analysis also justified the conclusion, as given in the following.

The typical bottom surface fracture morphology of the spalled ceramic coating piece (in Fig. 4) was shown in Fig. 5(a) and (b). There were many micro cracks and pores on the fracture surface. Both figures contained many irregularly shaped pores and inter-splat boundaries. The pore shape and size were completely

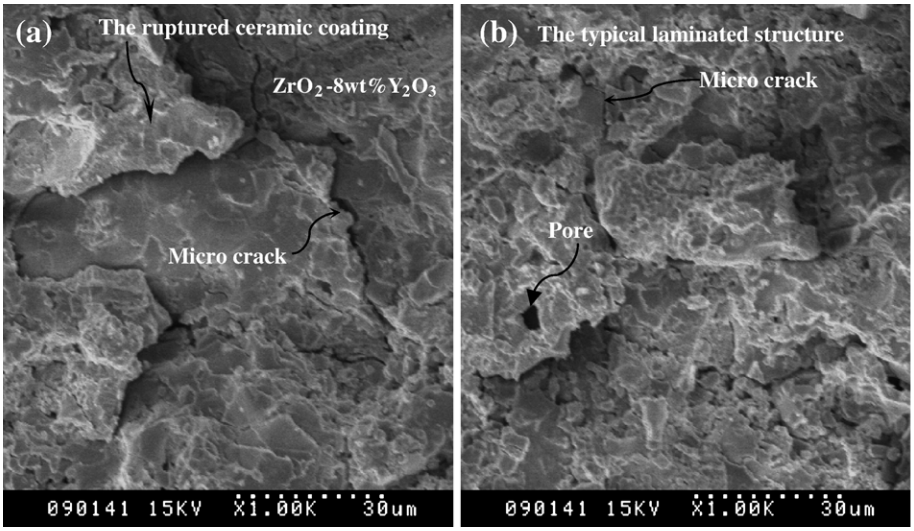

Fig. 5. (a) and (b). SEM micrographs of the fracture morphology of the bottom surface spalled ceramic coating piece after the buckling delamination failure. It is clearly many irregularly shaped pores and inter-splat boundaries are completely random.

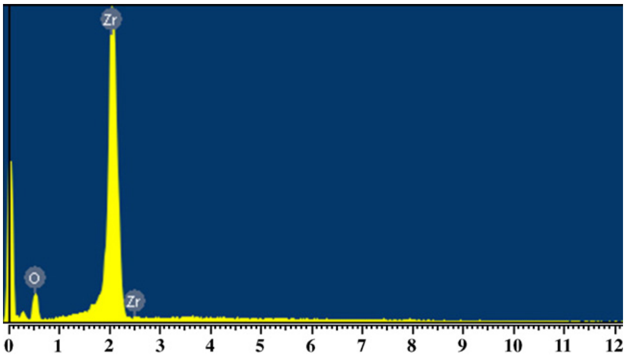

Fig. 6. The EDX spectrum of the bottom surface of the spalled ceramic coating piece.

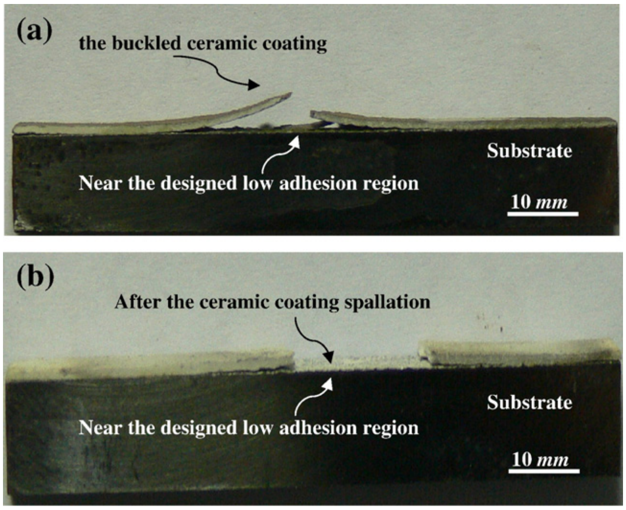

Fig. 8. (a) and (b). The other buckling delamination failure modes, where $P=2kN$, $L=10$ mm, $T_1=1280$ °C and $T_2=915$ °C in (a) and $P=2kN$, $L=8$ mm, $T_1=277$ °C and $T_2=214$ °C in (b).

random. Experimental observations indicated that some of these cracks coalesced to form large-scale delaminations susceptible to buckling. The fracture morphology was a typical sandwiched or laminated structure.

In order to identify the buckling delamination location of TBCs sample, the bottom surface region of the spalled ceramic coating piece shown in Fig. 5(a) was examined by EDX. It was shown in Fig. 6 that the material components are all 8 wt.% Y_2O_3–ZrO_2 materials, which meant that the fracture location lay within the ceramic coating just above the TBC/TGO interface. For plasma-sprayed coatings, buckling and spallation usually occurred in the ceramic coating, just above the TGO to ceramic interface [22,23]. The experimental results agreed with previous investigations.

The exposed substrate surface at the centre region of the TBCs sample in Fig. 4 was also examined by SEM. There were some micro-cracks and voids, as shown in Fig. 7. It indicated that a thin remnant 8 wt.% Y_2O_3–ZrO_2 coating adhered to the bond coat. It was clearly seen that the largest width of micro crack was 3 μm or more. In the presence of a sufficient thermal gradient, cracks formed and propagated on delamination planes in the TBC parallel to the interface, resulting in regions that spall away, leaving a thin layer of zirconia still attached to the substrate. These observations were consistent with other studies [10] which showed that the failure occurs within YSZ about 100-μm away from the interface for the as-sprayed specimen. The thermal cycles have only caused the failure location to shift from within the YSZ and about 100-μm away from the interface to near the interface.

The other buckling delamination modes were observed, as shown in Fig. 8(a) and (b). The fracture conditions for Fig. 8 (a) and (b) were, respectively, $P=2kN$, $L=10$ mm, $T_1=1280$ °C, $T_2=915$ °C and $P=2kN$, $L=8$ mm, $T_1=277$ °C and $T_2=214$ °C. For Fig. 8(b), the fracture conditions indicated that the buckling delamination failure phenomena of the TC did not occur at high temperature, but on cooling. The reason may be that the residual stress in the TC was compressive on cooling to ambient due to thermal expansion coefficient misfit. The magnitude of residual compressive stress in the TC gradually accumulated with thermal

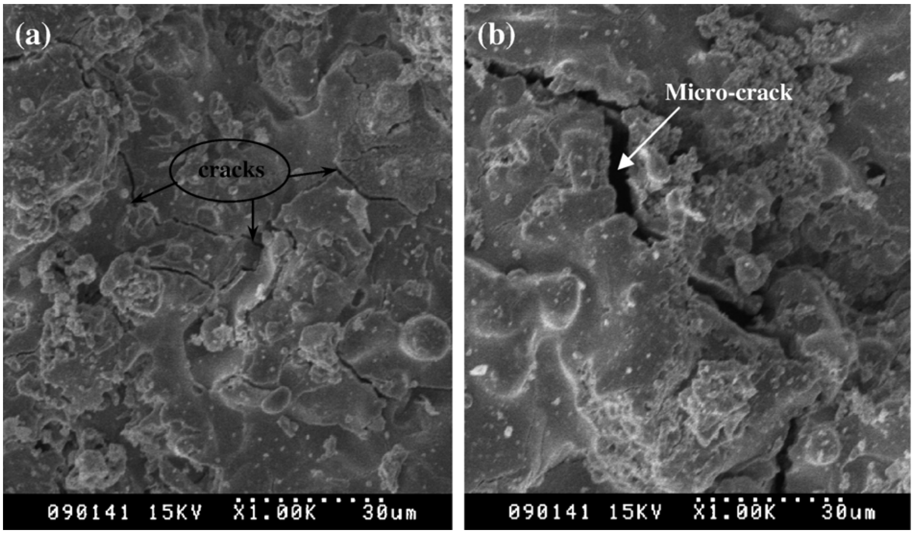

Fig. 7. (a) and (b). The surface microstructure of the exposed bond coat after the spallation of the ceramic coating. The thin ceramic coating still adheres to the bond coat and extensive cracking is apparent.

cycles [25–29]. Once the accumulated stresses (including residual stress and external mechanical stress) reached or exceeded the critical delamination buckling stress of the TC layer, the delamination buckling or spallation fracture would occur [24].

To clearly observe and determine the buckling delamination fracture location, the cross-sectional morphologies of the two buckled samples were carefully polished and identified by SEM. Fig. 9(a) denoted the cross-sectional morphology of the ruptured sample near the low adhesion region (see Fig. 8(a)). The maximal buckling deflection was about 1.8 mm. Fig. 9(b) was magnified from the dashed round region of Fig. 9(a). It was obviously seen that a very thin remnant 8 wt.% Y_2O_3–ZrO_2 layer kept adhering to the bond coat. The thickness of the residual TC layer is approximately 20 μm. The cross-sectional microstructure of the right buckled part of the samples (in Fig. 8(b)) was shown in Fig. 9(c). The dashed arrow represented the propagation direction of the delamination buckling. The propagation path trajectory of the delamination buckling was marked by the real line arrow. It was found that the interface crack was divided into two parts, i.e. one longitudinal crack continuing along the interface, the other transverse crack propagating forward the TC surface vertical to the interface. The former mainly propagated within the TBC parallel to the interface, as shown in Fig. 9(d). It was important that the latter transverse crack in the TC propagated from the TC interface to the TC surface and would eventually result in the spallation of the TC layer under thermal stress and mechanical stress. It was a very interesting conclusion which would be of great interest to study the delamination buckling failure mechanism of the TBCs system.

In all these experiments, the effect of the initial interface delamination length on the delamination resistance of the TBC system has been observed. If it was about 3 mm or less, the desired delamination buckling of the TC would be hard to occur in spite of the applied temperature magnitude. The global buckling failure of the system might occur when the mechanical loads at both edges were loaded to reach or exceed the critical bucking load of the substrate, as mentioned in Section 2 and discussed in Section 3.3. However, if the initial interface delamination length exceeded about 6 mm or more, the effect of

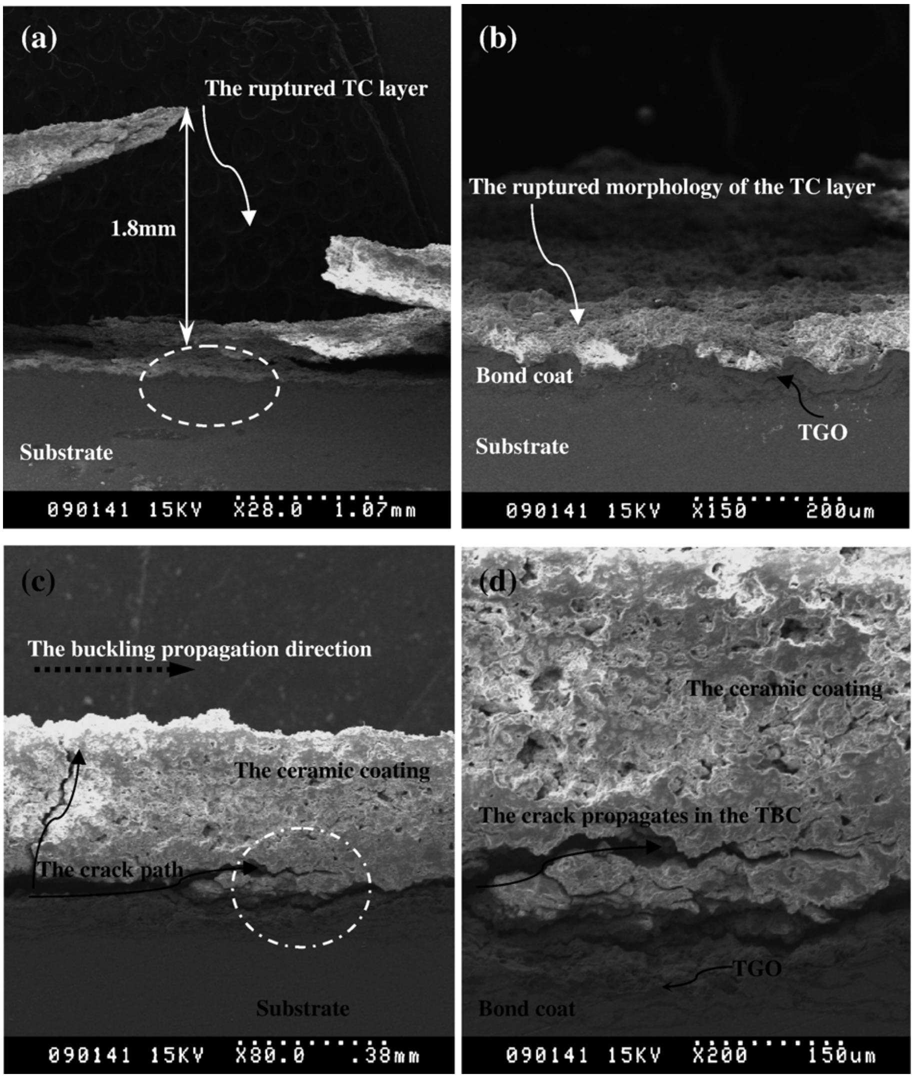

Fig. 9. The cross-sectional microstructures of the two samples (see Fig. 8) after delamination buckling failure at high temperature gradient. (b) and (d) are magnified from the dashed round region of (a) and (c), respectively. These micrographs are propitious to identify the buckling failure mechanism and fracture location.

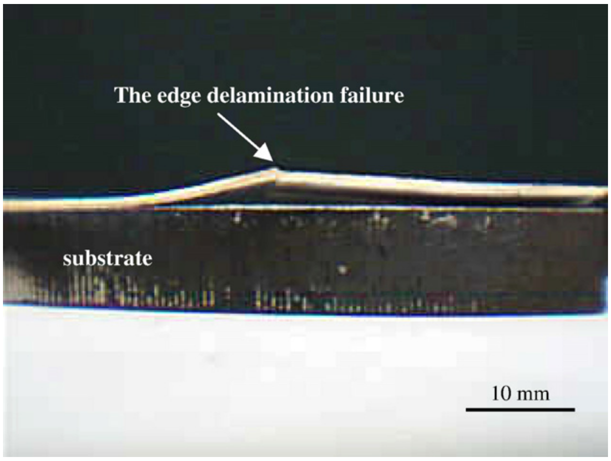

Fig. 10. The cross-sectional image of the through-width edge delamination failure of the ceramic coating under the coupled effects of thermal gradient and mechanical load, where $L=5$ mm.

it on the delamination resistance at the crack tip is of little significance, which have also been proved by other theoretical studies [24]. During the process of the delamination buckling, the buckling failure velocity of the ceramic coating was very fast. The interface delamination rapidly nucleated and propagated within the TBC close to the TBC/TGO interface. It was difficult to observe the postbuckling fracture behaviour of the TC because the ceramic coating was typically brittle material.

3.2. Typical edge delamination failure mode

A few through-width edge delamination failures were observed during the tests. Fig. 10 represented that the edge delamination failure of the TC occurred when $P=2kN$, $L=5$ mm, $T_1=1420$ °C and $T_2=1015$ °C. An initial edge flaw of sufficient magnitude near the TBC/TGO interface might serve to nucleate an edge delamination which quickly spread as a plane strain interface crack. The edge delamination length and maximal deflection were about 30 mm and 3 mm, respectively. Fig. 11(a) showed the other edge delamination failure image of the delaminated TBCs system, where $P=2kN$, $L=8$ mm, $T_1=1290$ °C and $T_2=992$ °C. The maximum deflection and length of the edge delamination reach about 5 mm and 22 mm, respectively.

This type of edge delamination configuration was compared with the theoretical schematic drawing [3,5], as shown in Fig. 11(b). Using the recorded data and Eqs. (1), (5), the mode II fracture toughness (Γ_i^{II}) in the TC layer at the crack tip approximately equalled to 35 J m^{-2}. The energy release rate (G_{ss}^{edge}) and stress intensity factor (K_{II}) were, respectively, about 38.8 J m^{-2} and 0.97 MPa $\sqrt{m}$ when the TC spalled from the bond coat at high temperature. The temperature-dependent material properties in TBCs samples were referred from literature [26]. It was seen that the energy release rate had exceeded the fracture toughness of the TBC when the delamination buckling failure of the TBC occurred. As a key condition, the magnitude of the energy release rate played an important role and it would determine whether the initial interface flaws could nucleate and propagate to interface delamination, with subsequent buckling and spalling. The magnitude of the SIF was close to the experimental results ($K_{\mathrm{IIc}}=0.65\pm0.04$ MPa $\sqrt{m}$ at 1316 °C in [30], $K_{\mathrm{IIc}}=1.0$–2.5 MPa $\sqrt{m}$ at ambient in [23]). Compared with previous investigations, Aktaa et al. have evaluated the delamination strength of the TBC system by fracture mechanics and finite element (code ABAQUS) approach. The TBC system consisted of a plasma-sprayed top coat of ZrO_2 8 wt.% Y_2O_3 (YSZ), a thermally grown oxide (TGO), a MCrAlY bond coat and an Inconel 617 substrate. The magnitude of the energy release rate was strongly influenced by thermal cycle phases, sinusoidal wavy interface roughness amplitude and crack length. They obtained that the magnitude of the mode-two energy release rate (G_{II}) varied from 15 to 50 J m^{-2} under different conditions [31]. For the similar TBC system, Semenov et al. have performed the finite element analysis of TBC delamination. The calculated the critical interface fracture toughness (G_c) of TBC delamination was approximately 36 J m^{-2}. The energy release rate changed with crack length and shrinkage strain. It also ranged from 10 to 100 J m^{-2}, as shown in Fig. 13 in the reference [32]. Hutchinson et al. have simulated the magnitude of energy release rates with a steady state (G_{ss}) for the interface delamination of TBC system. G_{ss} equals approximately to 40 J m^{-2} when the thermal gradient of the TBC system (ΔT) was 1135 °C [16]. Clyne et al. have measured the interfacial fracture energy of various interfaces within multilayer TBC

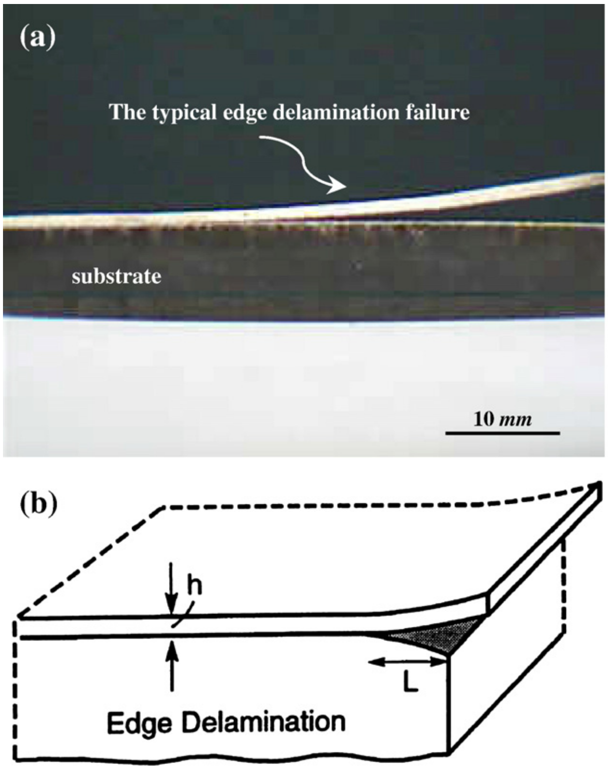

Fig. 11. (a) The through-width edge delamination failure of the ceramic coating under thermal gradient and compression load, where $P=2kN$, $L=8$ mm, $T_1=1290$ °C and $T_2=992$ °C. (b) A prevalent edge delamination mechanism for compressed coatings, which spreads from an edge to reveal the separation, as used in the prior investigations [3,5].

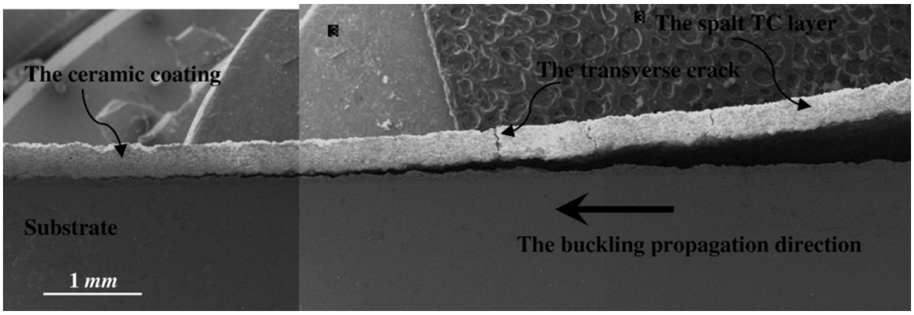

Fig. 12. The polished cross-sectional microstructures near the low adhesion region of the edge delaminated samples shown in Fig. 11(a). It is clearly seen that a few transverse cracks propagate vertical to the interface in the TC layer.

systems by using four-point bending test. The interface fracture energy (i.e. interface delamination strength) at the ZrO_2/NiCrAlY interface is about 40 J m^{-2}. The interface fracture energy at the ZrO_2/Al_2O_3 interface equals approximately 35 J m^{-2} [33]. Although the TBCs system and aging time are slightly difference, the trends are quite similar to our experimental results.

The edge delaminated sample in Fig. 11(a) was carefully polished and observed by SEM. Fig. 12 denoted the polished cross-sectional microstructures near the low adhesion region of the sample. It was clearly seen that a few transverse cracks propagated vertical to the interface in the TC layer. The longitudinal interface delamination continued to penetrate within the TC layer toward the “weakest” region. To identify the edge delamination fracture location at the interface, the two opposite fracture surfaces and various cross-sections of each broken sample were observed by SEM and EDX, as shown in Fig. 13. The bottom fracture surface of the spalled ceramic coating showed in Fig. 13(a) was examined by EDX, which represented that the material component were all yttria stabilized zirconia material. Since the fracture location lay within the TBC close to the TBC/TGO interface, the fracture morphology was similar to that of buckling delamination discussed above. There were also many micro cracks and voids in both figures. It seemed to be typical sandwiched or laminated structure. It was seen that the fracture surface of the edged-delamination in the delaminated TBCs specimen exhibited mainly inter-splats fracture mode. The delamination crack mainly propagated in the ceramic coating after the thermal aging for 200 h because the ceramic coating/bond coat interface maintains high strength in comparison to the TBC [23]. These observations are consistent with other experimental results.

3.3. Global buckling failure mode

The buckling delamination failure of the TBC sample would be the global buckling failure of the substrate rather than that of the TC layer when the initial interface delamination length was too small, e.g. 3 mm or less. Fig. 14 showed that the global buckling failure of the TBC system. The spallation of the TC mainly resulted from the buckling failure of the substrate. The experimental results substantially proved that the interface delamination length must be large enough (about several millimeter) to induce the nucleation of buckling delaminations or edge delaminations, which agreed well with the theoretical results [5,26,34].

Thus, for thermal barrier ceramic coating system, the interface delamination failure was mainly influenced by the

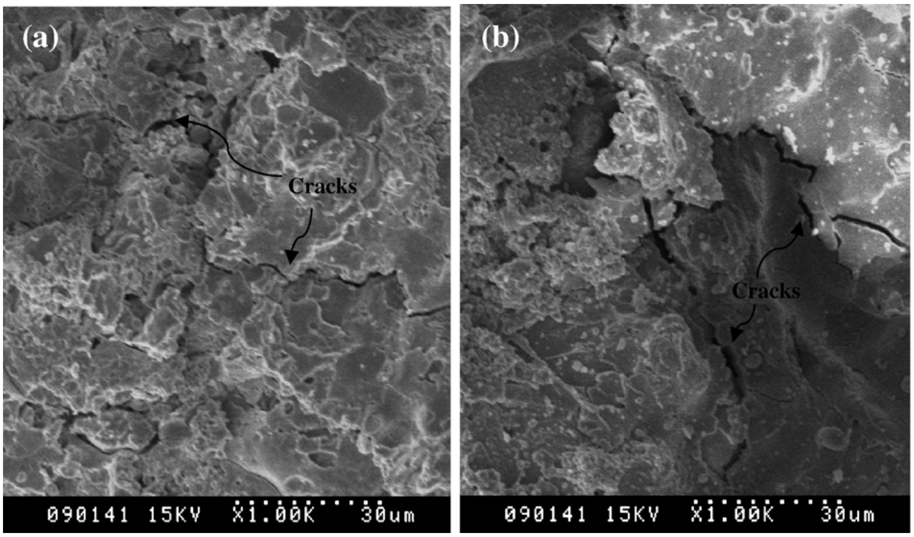

Fig. 13. The edge delamination fracture microstructures of the TBC sample. (a) The SEM image of the bottom surface of the spalled ceramic coating, (b) The SEM image of the exposed substrate surface.

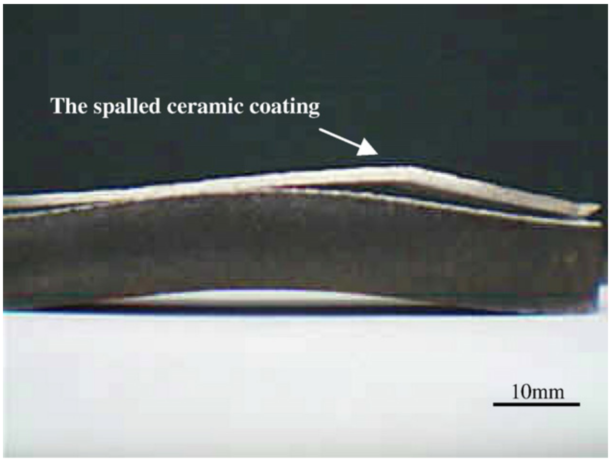

Fig. 14. The global buckling failure of the TBCs specimen occurs when the compression load exceeds the critical buckling loads of the substrate.

following factors, such as the coating stress, coating/substrate adhesion strength, interface flaw, initial interface delamination length and external loadings. Under compressive tests in this work, if the interface adhesion near the designed low adhesion region was lower than that at both edge regions, the failure phenomena of the TBC samples might be delamination buckling rather than edge delamination. But there was a large enough flaw existed in the TBC at both edges, the edge delamination would firstly occur. In this paper, the experimental conditions were designed to simulate thermal loadings that were encountered in the combustion chamber of a turbine by adjusting the distance between the torch and TC surface. With SEM observations, the interface buckling delamination initiated just above the designed low adhesion region and propagated within the TBC parallel to the interface due to thermal stress and mechanical stress. During the propagation process, the delamination tip began to divide into two orthogonal crack paths, as shown in Figs. 9(c) and 12. The transverse crack branching penetrated from the interface to the surface and would rapidly result in the spallation of the TC layer. It might be an important failure mechanism of delamination buckling of the ceramic coating. Furthermore, it was found that the buckling failure location lay within the TC layer and about 10~30 microns away from the interface for both delamination buckling and edge delamination failure. Although the failure mechanism investigation of a TBC, which is strongly influenced by the complicated service environments and external mechanical loading, is very difficult to clarify, it is believed that more research work is required in the near future. The function of a TBC is to protect metallic substrates from high temperature erosion and the thermal resistance of the coating is also an important consideration.

4. Conclusions

The primary purpose of this paper is to the buckling delamination and edge delamination failure characteristic of the TBC samples. Both delamination failure have been observed and discussed under the thermo-mechanical compressive tests at high temperature. The primary conclusions were summarized as follows,

1) The TBCs samples with a through-width interface pre-delamination were firstly designed and prepared by plasma sprayed technique. Their feasibility has been proved under compressive tests at high temperature.
2) It was found that the effect of the initial delamination length on the buckling failure characteristic played an important role. It was difficult to observe the delamination buckling of the TC layer if the initial length was too small, e.g. 3 mm or less. But the influence of the initial length on buckling failure would disappear when it reached 6 mm or more. Furthermore, the delamination buckling of the TC layer occurred not only at high temperature under thermo-mechanical loads, but also on cooling from high temperature to room temperature. Furthermore, the spallation of the TC layer was induced by the transverse crack branching which initiated and propagated from the interface to the surface.
3) For edge delamination failure in heat treated samples, the fracture toughness, energy release rate and stress intensity factor were evaluated and equalled to, respectively, 35 J m^{-2}, 38.8 J m^{-2} and 0.97 MPa $\sqrt{m}$ at high temperature gradient. These results are consistent with other previous studies. Once the delamination energy release rate exceeded the fracture toughness, the sufficient magnitude edge flaw might serve to nucleate an edge delamination, with subsequent spalling.
4) By SEM observations and EDX analysis, the fracture location at the interface was identified, and found to be within the TBC close to the TBC/TGO interface for both buckling delamination and edge delamination failure.

Acknowledgements

This work was supported in part by the Open Project Program of Key Laboratory of Low Dimensional Materials & Application Technology, Ministry of Education, China (No: KF0503) and by Scientific Research Fund of Hunan Provincial Education Department, China (No: 05C096). The authors also acknowledge the financial support provided by the Fund for Prominent Young Scholars from the Organization of NNSF of China (No: 10525211) and the Emphases Item of the NNSF of China (No: 50531060).

References

[1] N.P. Padture, M. Gell, E.H. Jordan, Science 296 (2002) 280.
[2] M.Y. He, J.W. Hutchinson, A.G. Evans, Prog. Mater. Sci. 46 (2001) 249.
[3] A.G. Evans, D.R. Mumm, J.W. Hutchinson, Prog. Mater. Sci. 46 (2001) 505.
[4] Y.C. Zhou, T. Hashida, Int. J. Fatigue 24 (2002) 407.
[5] J.W. Hutchinson, M.Y. He, A.G. Evans, J. Mech. Phys. Solids 48 (2000) 709.
[6] T. Patterson, D.I. Orloff, F. Bloom, Math. Comput. Model. 35 (2002) 165.
[7] M. Parlapalli, D. Shu, Eng. Struct. 26 (2004) 651.
[8] L. Wu, Compos. Struct. 64 (2004) 211.
[9] M. Gell, L. Xie, E.H. Jordan, N.P. Padture, Surf. Coat. Technol. 188 (2004) 101.
[10] L.L. Shaw, B. Barber, E.H. Jordan, M. Gell, Scr. Mater. 39 (1998) 1427.

[11] G. Thurn, G.A. Schneider, H.A. Bahr, F. Aldinger, Surf. Coat. Technol. 123 (2000) 147.

[12] H. Brodin, M. Eskner, Surf. Coat. Technol. 187 (2004) 113.

[13] D. Zhu, R.A. Miller, NASA TP3676, National Aeronautics and Space Administration, Glenn Research Center, Cleveland, OH, 1997.

[14] M.W. Moon, J.W. Chung, K.R. Lee, K.H. Oh, R. Wang, A.G. Evans, Acta Mater. 50 (2002) 1219.

[15] J.W. Hutchinson, Z. Suo, Adv. Appl. Mech. 29 (1992) 63.

[16] J.W. Hutchinson, A.G. Evans, Surf. Coat. Technol. 149 (2002) 179.

[17] J. DeMasi, K.D. Sheffler, M. Ortiz, NASA CR 182230, Pratt & Whitney, 1989.

[18] S.M. Meier, D.M. Nissley, K.D. Sheffler, NASA CR 189111, Pratt & Whitney, 1991.

[19] S.M. Meier, D.M. Nissley, K.D. Shelffler, S. Bose, J. Eng. Gas Turbine Power 114 (1992) 258.

[20] J.T. DeMasi-Marcin, K.D. Sheffler, J. Eng. Gas Turbine Power 112 (1990) 521.

[21] M. Gell, E. Jordan, K. Vaidyanathan, et al., Surf. Coat. Technol. 120 (1999) 53.

[22] J.T. DeMasi-Marcin, K.D. Sheffler, S. Bose, J. Eng. Gas Turbine Power 112 (1990) 521.

[23] Y. Yamazaki, A. Schmidt, A. Scholz, Surf. Coat. Technol. 201 (2006) 744.

[24] W.G. Mao, Y.C. Zhou, Adv. Mat. Res. 9 (2005) 31.

[25] V. Teixeira, Surf. Coat. Technol. 146 (2001) 79.

[26] W.G. Mao, Y.C. Zhou, L. Yang, X.H. Yu, Mech. Mater. 38 (2006) 1118.

[27] M.Y. He, J.W. Hutchinson, A.G. Evans, Mater. Sci. Eng., A Struct. Mater.: Prop. Microstruct. Process. 00 (2002) 1.

[28] A.M. Huntz, S. Daghigh, A. Piant, J.L. Lebrun, Mater. Sci. Eng., A Struct. Mater.: Prop. Microstruct. Process. 248 (1998) 44.

[29] M. Bäker, J. Rösler, G. Heinze, Acta Mater. 53 (2005) 469.

[30] S.R. Choi, D. Zhu, R.A. Miller, Eng. Fract. Mech. 72 (2005) 2144.

[31] J. Aktaa, K. Sfar, D. Munz, Acta Mater. 53 (2005) 4399.

[32] A.S. Semenov, H.-A. Bahr, H. Balke, H.-J. Weiss, Thin Solid Films 471 (2005) 200.

[33] T.W. Clyne, S.C. Gill, J. Therm. Spray Technol. 5 (1996) 401.

[34] S.R. Choi, J.W. Hutchinson, A.G. Evans, Mech. Mater. 31 (1999) 431.

Key Engineering Materials Vols. 353-358 (2007) pp. 239-242
online at http://www.scientific.net
© (2007) Trans Tech Publications, Switzerland
Online available since 2007/09/10

An Experimental Investigation of Interface Fracture Characteristic of APS Thermal Barrier Coating System under Bending at 1000 ^{o}C

W. G. MAO[1, 2], C. Y. DAI[1, 2], Y. C. ZHOU[1, 2, a] and Q. X. LIU[1, 2]

[1]Faculty of Materials & Optoelectronics Physics, Xiangtan University, Hunan, 411105, China

[2]Key Laboratory of Low Dimensional Materials & Application Technology, Ministry of Education, Xiangtan University, Hunan, 411105, China

[a]zhouyc@xtu.edu.cn

Keywords: Thermal barrier coatings; Three-point bending test; Interface fracture.

Abstract. This paper investigated the thermo-mechanical bending failure characteristic of air plasma-sprayed (APS) thermal barrier coating (TBC) system at 1000 ^{o}C by three-point bending test. A through-width surface pre-crack on the centre surface of the top ceramic coating (TC) in TBC sample was firstly designed and made by air plasma spraying technology. The fracture characteristic and spallation phenomena of the TBC were investigated under bending test in air at 1000 ^{o}C. The effects of constant displacement rate, span width of bending equipment and thermal aging time on the thermo-mechanical bending failure of the APS TBC system were slight at 1000 ^{o}C. Using SEM observations and EDX analysis, the interface cracks initiation, propagation and coalescence were discussed in detail. Furthermore, the fracture surface located within the TBC close to the TBC/TGO interface for all APS TBC samples under bending at 1000 ^{o}C.

Introduction

Thermal barrier coating (TBC) system of high-temperature components is required in power generating units for preventing the surface of the components from excessive heating, erosion and corrosion during the operation [1]. A typical TBC system is composed of a top ceramic coating (TC), a thermally grown oxide (TGO) that forms and thickens as the system cycles, bond coat (BC) that provides the oxidation resistance, and the substrate. However, various failure modes have been observed during the applications due to the harsh environment and great difference in the thermo-mechanical properties of the TBC system. one of the most common failure modes is cracking at the TC/TGO or TGO/BC interface leading to buckling delamination and spalling [2, 3], which may result in the degradation and fracture of TBCs. It is important to evaluate and predict the lifetime of TBC systems. The interface fracture behaviour and delamination resistance of plasma-sprayed zirconia coating were widely investigated by bending tests and tensile tests at room temperature [4-6]. Parts of them have studied the influence of treatment temperature and experimental temperature on the crack nucleation and propagation of the TBCs system. The crack density defined by the ratio of multiple crack numbers to the distance was often introduced to qualitatively measure the interface adhesion resistance of the TBCs system.

However, the interface failure mechanism of the TBCs system is a complicated problem. The above experimental results were mainly obtained at room temperature. In this work, in order to study the interface fracture resistance of the ceramic coating, a pre-cracked TBC samples were prepared by APS technique. This paper studied the fracture characteristic of APS TBC system by three-point bending test at 1000 ^{o}C. JSM-6360LV scanning electron microscope (SEM) and Energy Dispersive X-Ray (EDX) were used to examine fracture location and morphology.

Experiment

TBC system and Specimen preparation. In this work, the TBC system consisted of a plasma-sprayed top coat (TC) of ZrO_2 8 wt.% Y_2O_3 (YSZ), a NiCrAlY bond coat and a SUS304 stainless steel substrate. The thickness, width and length of the substrate are, respectively, 1.8mm, 10mm and 150mm. To study the influence of the TC thickness (denoted h_c), there are three different values chosen, i.e. 200μm, 300μm and 400μm. A through-width pre-crack on the TC surface was designed and made by plasma-sprayed, which was benefit to study the interface fracture characteristic of the TBC system. The width of the pre-crack (denoted b) can be controlled by the temperature-resistance tape. The detailed process is shown in Fig.1. All TBC samples were performed different thermal aging time at 1000 ^{o}C, i.e. 48h and 100h. The thermal cycles consisted of 24 hours at 1000 ^{o}C with air cooling in laboratory air.

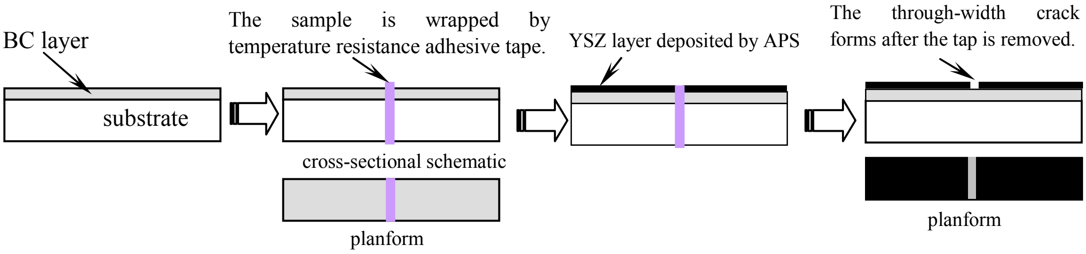

Fig. 1 The schematic for creating through-width surface crack of the TC layer.

Experimental procedure

Fig. 4 showed the schematic graph of the three-point bending equipment with 60 mm span width (denoted L). There were thirty samples tested in this work. Three pieces of thermocouples were used to measure, respectively, the top surface temperature of the ceramic coating, the bottom surface temperature of the TBC sample and the cross-sectional temperature of the TBC sample. Note that the torch flame only heated the TC surface rather than other surfaces. The oxyacetylene torch, whose axis was orthogonal to the TC surface, was translated at a constant velocity of 2 *cm/s* so that the TC surface could be heated uniformly. Furthermore, the maximal temperature of the TC surface was easily controlled within the range of 1000 ± 10 ^{o}C by adjusting the distance between the torch flame and the TBC surface. Every sample in each test was firstly heated up to about 1000 ^{o}C and remained for half an hour. And the compression load was loaded under constant displacement rate (denoted as v) of 10.0 *mm/min* until the spallation of the ceramic coating occurred completely. The interface crack nucleation, propagation and coating spallation were observed by an optical microscope and SEM.

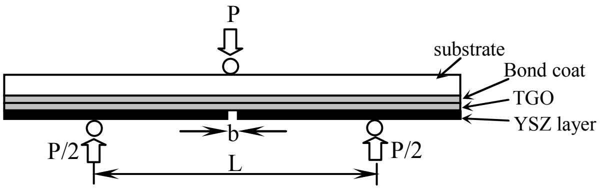

Fig. 2. The schematic drawing of the specimen geometry and three-point bending test in this work.

Results and Discussion

Although the difference of the pre-cracked TBC sample existed, *the experimental bending failure morphologies were almost identical in all tests at 1000 ^{o}C (for as-received and treated coated samples),* as shown in Fig. 3. The failure configuration seemed to be the tree bark structure. In order to understand these phenomena and mechanism, the constant displacement rate, applied temperature, span width and thermal aging time were adjusted from 0.5mm/min to 50mm/min, from room temperature to high temperature (e.g. 1400 ^{o}C), from 60 mm to 30 mm and from as-received to 100 h respectively, but these factors did not change the experimental results. The ceramic coating was not completely detached from the substrate. Furthermore, the pre-crack did not open completely under bending at 1000 ^{o}C. There were many parallel surface cracks existed on the TC surface due to tensile-shear stresses. These surface cracks vertically to the interface spread from the pre-crack location because the ceramic coating was placed in the bottom (opposite) site where the three-point bend indent was applied, as shown in Fig. 2, the ceramic coating section of the TBC specimen was subjected to tensile-shear force only. The development of external mechanical loading and high temperature gradient created local stress concentration in the surface centre region of the TC. As the loading conditions continued during the tests, crack initiation and propagation further extended in the coating and toward the coating/base material interface. Furthermore, the coating was deformed through multi-cracking, which indicated that coating did not conform to the plastic deformation produced in the substrate material. The multi-vertical cracks would kink out the macro interface cracks or delamination. The delamination cracks, parallel to the width of TBC sample, would coalesce and propagate due to tensile-shear loading. Eventually, the top ceramic coating (TC) would detach from the substrate. To identify the interface crack propagation and the spallation fracture location of the ceramic coating, the cross-sectional failure morphology of the TBC sample was polished and examined by SEM and EDX, as shown in Fig. 3(c).

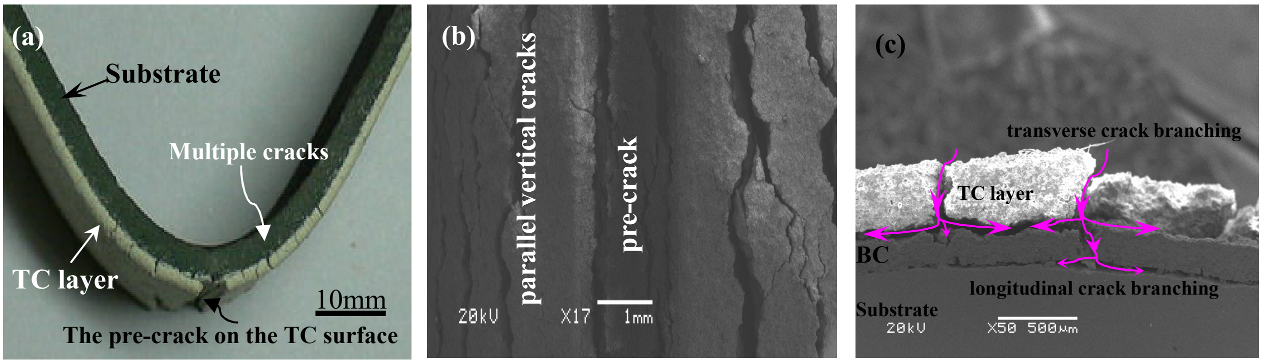

Fig. 3. The three-point bending failure photographs of the TBC specimen at 1000 °C.
(a) digital image, (b) SEM image of the surface morphology near the pre-crack.
(c) SEM images of the polished cross-section morphology

It was clearly observed from Fig.3(c) that many multiple micro transverse cracks firstly initiated and gradually passed the TC with the increase of bending load. All these cracks were divided into three main crack branchings close to the TBC/BC interface. Both of them propagated within the TC near the TC/TGO interface. The other crack branching penetrated vertically into the BC layer and reached at BC/Substrate interface. But the crack front did not penetrate the substrate. This branching was divided again into two small branching which propagated within the BC layer close to the BC/Substrate interface. It was found that the typical crack path trajectory in the TBC sample grew between the TBC/BC or BC/Substrate interfaces. The substrate revealed substantial deformation twins in this work. It indicated that the spallation of the ceramic coating was mainly induced by the two longitudinal crack branching which propagated within the TC layer close to the TC/TGO interface. This point would be further proved in the following discussion.

To identify the failure location at the interface, the two opposite fracture surfaces and various cross-sections of each broken specimen were examined using SEM and EDX. Fig. 4 shows the SEM image of the bottom fracture surface morphology of the spalled part after bending test at 1000 oC. It is noted that the fracture surface on the bond coat side (Fig. 4(a)) contains many parallel surface cracks, whereas the fracture surface on the TBC side (Fig. 4(b)) contains a few macro-cracks. This bottom surface of the spalled part (in Fig. 4(b)) was examined by EDX and its component was all YSZ material, which proved that the fracture surface located within the TBC close to the TBC/TGO interface. The similar results were also found in other bending tests.

Conclusions

The aforesaid study leads to the following conclusions , (a) the TBC sample with a through-width surface pre-crack on the top ceramic coating was firstly designed and made by using plasma sprayed technique. (b) The thermo-mechanical bending failure characteristics of the TBC system had been investigated in bending tests at 1000 °C. It was found that all bending failure morphologies were almost identical. The ceramic coating did not entirely detach from the substrate.

The effects of the constant displacement rate, experimental equipment span width and thermal aging time on the failure morphology were slight at 1000 °C. (c) Using SEM observations and EDX analysis, the interface cracks initiation, propagation and coalescence were discussed in detail. Furthermore, the fracture surface located within the TBC close to the TBC/TGO interface for all TBC samples under bending at 1000 °C.

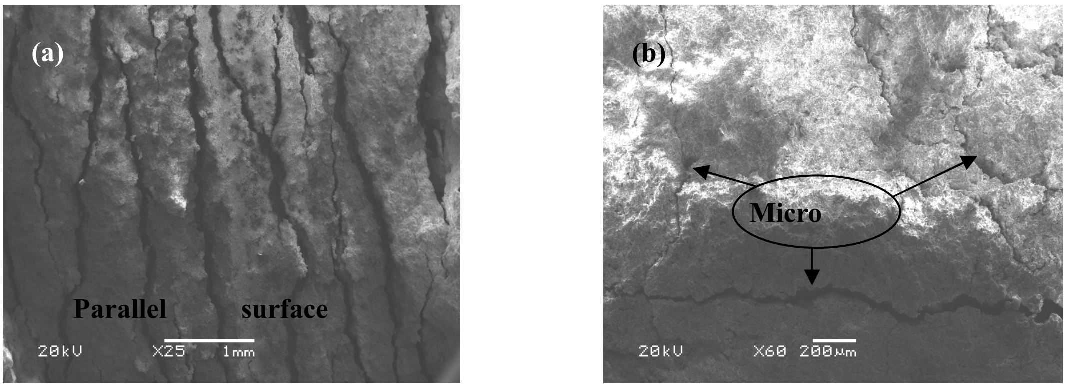

Fig. 4. SEM micrographs of the two opposite fracture surfaces of the heat treated TBC sample after bending test at 1000 °C. (a) bond coat surface, (b) underside of the spalled TBC

Acknowledgements

This work was supported in part by the Open Project Program of Key Laboratory of Advanced Materials & Rheological Properties, Ministry of Education, China (No: KF0503) and by Scientific Research Fund of Hunan Provincial Education Department, China (No: 05C096). The authors also acknowledge the financial support provided by the Fund for Prominent Young Scholars from the Organization of NNSF of China (No: 10525211) and the Emphases Item of the NNSF of China (No: 50531060).

References

[1] N.P. Padture, M. Gell, E.H. Jordan: Science Vol. 296 (2002), p. 280

[2] M.Y. He, J.W. Hutchinson and A.G. Evans: Progress Materials Science Vol. 46(2001), p. 249

[3] A.G. Evans, D.R. Mumm and J.W. Hutchinson: Progress Materials Science Vol. 46(2001), p. 505

[4] Y. Yamazaki, A. Schmidt and A. Scholz: Surface & Coatings Technology. Vol. 201 (2006), p. 744

[5] Y.C. Zhou, T. Tonomori, A. Yoshida, L. Liu, G. Bignall, T. Hashida: 2002, Surface and Coatings Technology, Vol. 157 (2002), p.118

[6] G. Thurn, G.A. Schneider, H. A. Bahr and F. Aldinger: Surface and Coatings Technology, Vol. 123(2000), p. 147

Advanced Materials Research Vol. 9 (2005) pp. 31-40
online at http://www.scientific.net

Failure of Thermal Barrier Ceramic Coating Induced By Buckling Due to Temperature Gradient and Creep

W. G. Mao and Y. C. Zhou[1]

Key Laboratory for Advanced Materials and Rheological Properties of Ministry of Education
Faculty of Materials & Optoelectronics Physics, Xiangtan University, Hunan, 411105, P.R. China
[1]zhouyc@xtu.edu.cn

Keywords: thermal barrier ceramic coatings, residual thermal stress, thermal cycle, buckling failure

Abstract. The intent of this article was to study the failure mechanism of thermal barrier coatings (TBCs) induced by buckling. The main content included the following two parts. The first part investigated the thermal residual stresses fields in TBCs with thermal cycles, which induced by the non-linear coupled effect of temperature gradient, thermal fatigue and creep strain of TBCs. One found that the residual stresses in ceramic coating were compressive and accumulated with thermal cycles, which may be high enough to induce the buckling failure of ceramic coating. The second part studied the critical buckling failure loading of the ceramic coating in TBCs under the condition of the compressive loading by use a theoretical model. Finally, a buckling plane, i.e. $n-T_s$ plane, was obtained by combined the above sections and applied to predict the buckling failure of the TBCs system. In this plane, it was divided into the two parts, i.e., non-buckling region and buckling region.

Introduction

The TBCs system consisting of ceramic coating, bond coat and substrate was now employed in most turbine engines, permitting gas temperature to be raised substantially above those for uncoated systems [1,2]. The ceramic coating (i.e.7-9wt% yttria stabilized zirconia) could protect the turbine components due to its low thermal conductivity and diffusivity as well as its acceptable thermal shock resistance. However, there are many factors that can degrade the thermal function of the TBCs. Zhou and Evans et al. have reviewed the mainly failure mechanisms of the TBCs system [3,4,5,6]. The oxidation at the interface of ceramic coating/bond coat at high temperature may result in the interface delamination [7,8,9]. The accumulated residual stresses and the oxidation in TBCs may result in the buckling and spallation failure of the ceramic coating [10].

In this paper, the thermal residual stresses in TBCs are firstly studied during thermal cycles. After that, a theoretical model is proposed to predict the critical buckling loading of the ceramic coating under the condition of the compressive loading.

Thermal Residual Stresses Field in TBCs

The deformation of the ceramic coating is assumed to be elastic and creep. The deformation of bond coat and substrate are regarded as elastic [3,11]. Furthermore, due to the fact that the material properties of bond coat and substrate are very close, they will be regarded as a layer and named as substrate, as shown in Fig.1.

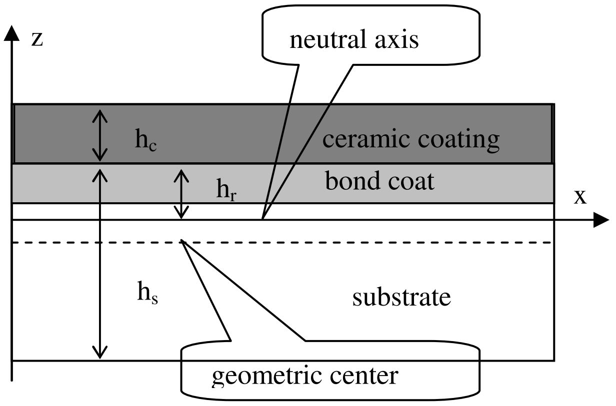

Fig.1. Schematic of the crossing-section view of the TBC system.

The stress-strain fields of each layer in TBCs are determined incrementally during the heating, holding temperature and cooling period. They can be written as follows,

$$d\varepsilon_{ij}(z,t) = de^e_{ij}(z,t) + \delta_{ij}d\varepsilon + \delta_{ij}\alpha(T)dT(z,t) + d\varepsilon^c_{ij}(z,t)\,. \tag{1}$$

where the de^e_{ij} represents the deviator strain increment components, δ_{ij} and $d\varepsilon_m$ represent the Kronecker delta and mean strain increment, respectively. $\alpha(T)$ denotes thermal expansion coefficient. In equation (1), $d\varepsilon^c_{ij}(z,t)$ is the creep increment of strain component. It can be written as [3,11],

$$d\varepsilon^c_{ij}(z,t) = F(t)f_1(z)A\times\exp(-Q/RT(z,t))\times(\sqrt{3J_2}/\sigma_0)^n\times(t/t_0)^{-s}\,dt\,. \tag{2}$$

where

$$F(t) = \begin{cases} 1 & 0 < t < t_2 \\ 0 & t_2 < t < t_3 \end{cases}. \tag{3}$$

$$f_1(z) = \begin{cases} 0 & -(h_s - h_r) < z < h_r \\ 1 & h_r < z < h_r + h_c \end{cases}. \tag{4}$$

In the above equations, A, Q, n and s are, respectively, material constant, creep activation energy, stress exponent and time exponent. J_2 is the second invariant of the deviator stress. R, T, t denote, respectively, gas constant, temperature and time. σ_0 and t_0 are the initial stress and reference time, respectively. In equation (3), the physical meaning of $t_i\,(i=1,2,3)$ denotes the different moment during the thermal cycle history, i.e. the heating time, holding time and cooling time, respectively. In equation (4), h_c and h_s are, respectively, the thickness of the ceramic coating and that of substrate. Due to the thermal expansion coefficients and other material properties mismatch in TBCs, the geometric axis and neutral axis don't superpose. The physical meaning of h_r is given in Fig.1 and it can be obtained as [12],

$$h_r = (E_s h_s{}^2 - E_c h_c^2)/2(E_s h_s + E_c h_c)\,. \tag{5}$$

where E_s and E_c denote, respectively, the Young's modulus of substrate and that of ceramic coating. Note that the material properties, such as thermal expansion coefficient, Young's modulus and Poisson's ratio are dependent on temperature. Moreover, temperature distribution in TBCs is assumed to be the linear function of the coordinate axial z [3]. Therefore, the temperature fields, $T(z,t)$, can be written in the following form,

$$T(z,t)=\begin{cases}(T_1(z)-T_0)\times t/t_1+T_0 & (0\le \mathrm{t}\le \mathrm{t}_1)\\ T_1(z) & (\mathrm{t}_1\le \mathrm{t}\le \mathrm{t}_2)\,.\\ T_1(z)-(T_1(z)-T_0)\times(t-t_2)/(t_3-t_2) & (\mathrm{t}_2\le \mathrm{t}\le \mathrm{t}_3)\end{cases} \tag{6}$$

where,

$$T_1(z)=\begin{cases}(T_s-T_b)\times z/h_c+(T_b-h_1\times(T_s-T_b)/h_c) & (h_1\le z\le h_1+h_c)\\ T_b & (h_1-h_s\le z\le h_1)\end{cases}. \tag{7}$$

Here T_0 and $T_1(z)$ denote, respectively, the ambient temperature and the temperature distribution in TBCs during the holding period, which is the function of position z. T_s and T_b denote, respectively, the highest temperature on the surface of ceramic coating and that of substrate.

The problem is assumed to be plane stress and the stresses are equi-biaxial stress state in the following analysis. The effect of bending moment on the stress distribution is neglected [11]. The deformation of each layer is assumed to satisfy the strain compatibility, mechanical equivalent and boundary condition at the edges of the TBCs system segment during the thermal cycles. Moreover, stress-strain relationship in TBCs is assumed to obey the Hooke's law during the cooling period. Eventually, thermal residual stress in TBCs at the end of cooling can be deduced by using the thermal stress theory and equivalent boundary method. The analytical solution can be obtained as follows,

$$\begin{aligned}\sigma_{residual(n)}(z,t)={}&\sigma_{residual(n-1)}(z,t)+\frac{E(T)}{1-\nu(T)}\times\Bigg[-\int_0^t\left(2B(z,t)f_1(z)F(t)(t/t_0)^{-s}+\alpha(T)dT(z,t)/dt\right)dt\\ &+\frac{\displaystyle\int_{-h_s+h_1}^{h_1+h_c}\left[\int_0^t\frac{E(T)}{1-\nu(T)}\left(\alpha(T)dT(z,t)/dt+F(t)f_1(z)B(z,t)(t/t_0)^{-s}\right)dt\right]dz+\int_{h_1}^{h_1+h_c}\int_0^t\frac{E_c(T)}{1-\nu_c(T)}F(t)f_1(z)B(z,t)(t/t_0)^{-s}dtdz}{\displaystyle\int_{-h_s+h_1}^{h_1+h_c}\frac{E(T)}{1-\nu(T)}dz}\Bigg]\\ &+\frac{E(T)}{1-\nu(T)}\times\left[-\int_{t_2}^{t}\alpha(T)(dT(z,t)/dt)dt+\frac{\displaystyle\int_{-h_s+h_1}^{h_1+h_c}\int_{t_2}^{t}\frac{E(T)}{1-\nu(T)}\times\alpha(T)(dT(z,t)/dt)dtdz}{\displaystyle\int_{-h_s+h_1}^{h_1+h_c}\frac{E(T)}{1-\nu(T)}dz}\right].\end{aligned} \tag{8}$$

where

$$B(z,t)=A\times\exp(-Q/RT(z,t))\times(\sqrt{3J_2}/\sigma_0)^n\,. \tag{9}$$

Note that the subscript n in equation (8) denotes thermal cycle number. In the second and subsequent cycles, the effect of the residual stress in TBCs produced in the last thermal cycle must be considered.

Model of the Buckling Failure

The calculated results in the following section will show that the accumulated residual stress in the ceramic coating is compressive and increases with thermal cycle. In addition, it is well known that the interface oxidation may result in interface delamination or crack during the thermal cycle. The buckling failure phenomenon of the ceramic coating may occur under the influence of the compressive residual stresses when the interface delamination/crack lengthens with thermal cycles. In this section, in order to predict the buckling failure of the ceramic coating, more attention will be focused on the relationship of the residual stress, interface delamination length, critical buckling loading and thermal cycle number.

Basic Assumptions. Fig. 2 is the schematic of the buckling failure of the ceramic coating. The interface is assumed to be an across-the-width delamination and the TBCs system is divided into four regions. Therefore, the simple beam theory can be used to study the buckling failure mechanism. Moreover, the materials are assumed to be homogeneous and isotropic. A mechanical force *P* is applied at the two edges of TBCs system and the load is used to approximately replace the compressive residual stress in the ceramic coating accumulated during thermal cycles. The interface between regions 2 and 3 could be delaminated, which means the weakest adhesion region. The interfaces in regions 1 and 4 represent the strong adhesion region, which can be regarded that the delamination/crack will not propagate along these interfaces in this paper. The delaminated TBCs system is assume to be clamped at the two edges.

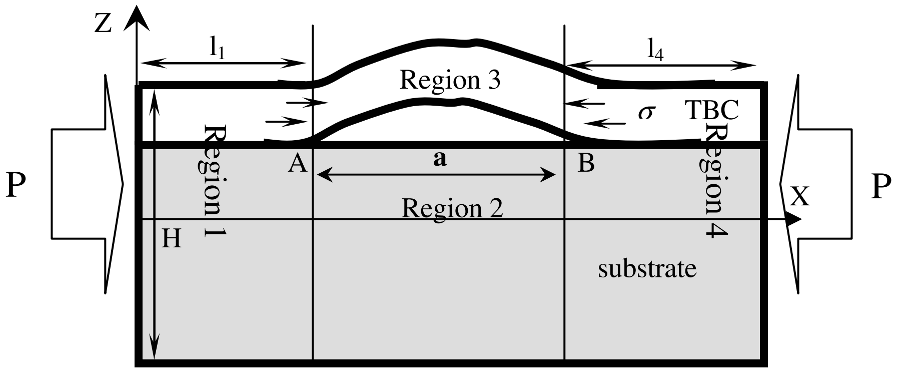

Fig.2. Schematic of the buckling failure of the ceramic coating in TBCs system under the condition of compressive stresses.

Balance Equations. The first order shear deformation theory is introduced to describe the displacement of each region and they can be written as follows [13],

$$\bar{u}_i(x_i,z_i)=u_i(x_i)+z_i\psi_i(x_i). \tag{10}$$

$$\bar{w}_i(x_i,z_i)=w_i(x_i). \tag{11}$$

where $\bar{u}_i(x_i,z_i)$ and $\bar{w}_i(x_i,z_i)$ are, respectively, the displacement in the x-direction and the deflection in the z-direction. $u_i(x_i)$ and $\psi_i(x_i)$ in equation (10) denote, respectively, the displacement of each region along the x direction and the rotation of the normal to the beam midplane. In equations (10) and (11), $x_i\in[0,l_i]$ and $z_i\in[-h_i/2,h_i/2]$ denote, respectively, the local axial coordinate and transverse coordinate of each region, where $z_i=z-d_i$ and $d_i=H/2-h_i/2$. Using Hooke's law and geometry equation, the strain energy and potential energy in each region can, respectively, be written as follows [13],

$$U_i = \frac{1}{2}\int [D_{0i}{u_{i,x}}^2 + D_{2i}{\psi_{i,x}}^2 + B_{0i}(\psi_i + w_{i,x})^2 + 2D_{1i}u_{i,x}\psi_{i,x}]dx_i\,. \tag{12}$$

$$V_i = -P_i\int \left(u_{i,x} + z_i\varphi_{i,x} + w_{i,x}^2/2\right)dx_i\,. \tag{13}$$

where D_{0i}, D_{1i}, D_{2i}, B_{0i} denote the stiffness coefficient matrix and the details are given in the reference [13]. In order to obtain the balance equations by *potential variational principle*, the displacement variables are divided into two parts,

$$u_i(x_i) = {u_i}^0(x_i) + {u_i}^a(x_i)\,. \tag{14}$$

$$\psi_i(x_i) = {\psi_i}^0(x_i) + {\psi_i}^a(x_i)\,. \tag{15}$$

$$w_i(x_i) = {w_i}^0(x_i) + {w_i}^a(x_i)\,. \tag{16}$$

where $\{{u_i}^0(x_i)\ \ {\psi_i}^0(x_i)\ \ {w_i}^0(x_i)\}$ is the displacement function of the initiate balance state and $\{{u_i}^a(x_i)\ \ {\psi_i}^a(x_i)\ \ {w_i}^a(x_i)\}$ is the small variables of the displacement function when the buckling failure phenomenon occurs in ceramic coating. The total potential energy is done by the two order variation, i.e.

$$\delta^2\Pi = \sum_{i=1}^{4}\delta^2\Pi_i = \sum_{i=1}^{4}\delta^2(U_i + V_i)\,. \tag{17}$$

Therefore, the balance equations in each region can easily be obtained,

$$D_{0i}{u_{i,xx}}^a + D_{1i}{\psi_{i,xx}}^a = 0\,. \tag{18}$$

$$D_{1i}{u_{i,xx}}^a + D_{2i}{\psi_{i,xx}}^a - B_{0i}({\psi_i}^a + {w_{i,x}}^a) = 0\,. \tag{19}$$

$$P_i{w_{i,xx}}^a - B_{0i}({\psi_{i,x}}^a + {w_{i,xx}}^a) = 0\,. \tag{20}$$

Boundary Conditions and Continuity Conditions. The boundary conditions on both edges can be given as follows,

$${u_1}^a = {\psi_1}^a = w_1^a = 0, \qquad for\ \ (x_1 = 0)\,. \tag{21}$$

$${u_4}^a = {\psi_4}^a = w_4^a = 0, \qquad for\ \ (x_4 = l_4)\,. \tag{22}$$

The displacement continuity at positions A and B shown in Fig. 2 must be satisfied and can be written as follows,

$$u_i^a(0) = u_1^a(l_1) + d_i\psi_1^a(l_1)\,. \tag{23}$$

$${\psi_i}^a(0) = {\psi_1}^a(l_1)\,. \tag{24}$$

$${w_i}^a(0) = {w_1}^a(l_1)\,. \tag{25}$$

$$u_i{}^a(l_i) = u_4{}^a(0) + d_i\psi_4{}^a(0)\,. \tag{26}$$

$$\psi_i{}^a(l_i) = \psi_4{}^a(0)\,. \tag{27}$$

$$w_i{}^a(l_i) = w_4{}^a(0)\,. \tag{28}$$

where the subscript i equals 2 and 3, respectively. To simplify the analysis in the following, the generalized forces of each region are defined as,

$$X_i(x_i) = D_{0i}u_{i,x}{}^a + D_{1i}\psi_{i,x}{}^a\,. \tag{29}$$

$$\phi_i(x_i) = D_{1i}u_{i,x}{}^a + D_{2i}\psi_{i,x}{}^a\,. \tag{30}$$

$$Z_i(x_i) = B_{0i}(\psi_i{}^a + w_{i,x}{}^a) - P_i w_{i,x}{}^a\,. \tag{31}$$

The continuity conditions of generalized forces at positions A and B can be written as follows,

$$X_j(l_{14}) = \sum_{i=2,3} X_i(l_{23})\,. \tag{32}$$

$$\phi_j(l_{14}) = \sum_{i=2,3} [d_i X_i(l_{23}) + \phi_i(l_{23})]\,. \tag{33}$$

$$Z_j(l_{14}) = \sum_{i=2,3} Z_i(l_{23})\,. \tag{34}$$

Here, $j = 1$ and $j = 4$ denote positions A and B, respectively. For point A, $l_{14} = l_1$, $l_{23} = 0$ and for point B, $l_{14} = 0$, $l_{23} = l_2$.

State-Space Method (SSM). The state space method is used to study the critical buckling failure loading of the TBCs system. The space state variable in each region is defined as,

$$\{\eta_i\} = \{u_i^a \quad \psi_i^a \quad w_i^a \quad u_{i,x}^a \quad \psi_{i,x}^a \quad w_{i,x}^a\}^T\,. \tag{35}$$

where "T" denotes the transposition of matrix in equation (35). Therefore, the governing balance equations (18), (19) and (20) in each region can be denoted by using the following form,

$$d\eta_i / dx_i = S_i\eta_i\,. \tag{36}$$

where S_i denotes the coefficients matrix and the detail is given in the reference [13]. The solution of the equation (36) can be obtained as follows,

$$\eta_i = e^{S_i x_i}\eta_i^0 = K_i(x_i)\eta_i^0\,. \tag{37}$$

where η_i^0 is an integral invariant matrix. All of the boundary conditions (21)-(22) and continuity conditions (i.e. from Eq. (23) to Eq. (28), from Eq. (32) to Eq. (34)) are rewritten in the state-space. Finally, the linear algebraic equations can be obtained as follows [13],

$$M\eta^0 = 0\,. \tag{38}$$

where $\eta^0 = \left\{\eta_1^0, \eta_2^0, \eta_3^0, \eta_4^0\right\}^T$ and the coefficient matrix M is defined in reference [13]. If an untrivial solution exists in equation (38), the determinant of its coefficient matrix must be equal to zero,

$$Det|M| = 0. \tag{39}$$

The lowest eigen value of the determinant of Eq. (39) is just the critical buckling loading.

Results and Discussion

Thermal Residual Stresses in TBC. The materials properties used in the calculation are temperature-dependent and taken from reference [3]. h_c and h_s are, respectively, 0.35*mm* and 2.1*mm*. The thickness of bond coat is 0.1*mm*. t_1, t_2, t_3 are equal to, respectively, *600s*, *4200s*, *4800s*. Substrate temperature, T_b, equals $700^0 C$. The highest surface temperature of the ceramic coating, T_s, is assumed to vary from $1000^0 C$ to $1600^0 C$. During the calculation, a finite difference approach was used to solve the equation (8). The temperature fields and stress fields in TBCs are determined incrementally during thermal cycles.

After TBCs experiences many thermal cycles, the thermal stresses distribution in ceramic coating are shown in Fig.3. It can be seen that the thermal stress in x-direction, i.e. $\sigma_{11}(z,t)$, at the end of holding period is tensile, where T_s equals $1000^0 C$. However, due to the effect of the last residual compressive stress, the tensile thermal stress at the end of holding time decreases with the increase of thermal cycles. The thermal tensile stress at ceramic coating/bond coat interface is far larger than that on the top surface of ceramic coating. Moreover, when thermal cycles *n* equals 15, the thermal stress on the top surface of ceramic coating equals approximately zero and this decrease is due to the influence of creep deformation and stress relaxation in ceramic coating. The results are in a good agreement with the experimental results as reported by Zhu et al.[11].

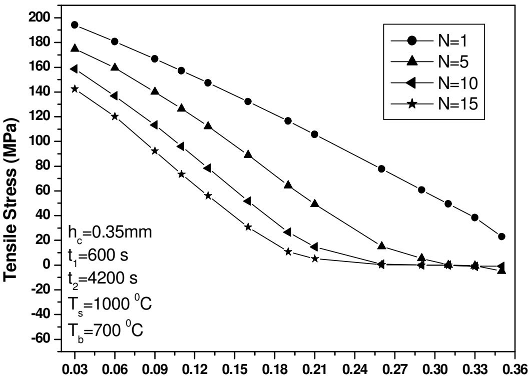

Fig.3. The relationship of thermal stress in ceramic coating at the end of holding time with thermal cycles.

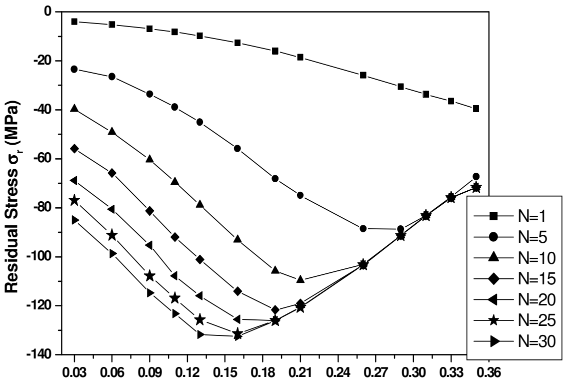

Fig.4. The relationship of residual stress in ceramic coating at the end of cooling time with thermal cycles.

The relationship of residual stress in ceramic coating at the end of cooling with position *z* for different thermal cycles *n* is shown in Fig.4, where the temperature on the surface of ceramic coating T_s is $1000^0 C$. It is seen that the residual stresses at ceramic coating/bond coat interface increase with the increase of thermal cycles. Especially, the residual stress is compressive. When the TBCs experiences 30th thermal cycles, the largest compressive residual stress is up to $-134MPa$. However, the residual stresses on the top surface of ceramic coating are close to $-70MPa$. As we know, the surface temperature of the top coating is much higher than that at the interface. Therefore, the creep strain on the surface of the top ceramic coating is much higher than that at the interface. Finally, the stress relaxation induced by the creep strain of ceramic coating may occur on the surface of the ceramic coating [11,13].

Fig.5 shows the relationship of the residual stresses at the ceramic coating/bond coat interface with thermal cycles for different temperature on the surface of the top ceramic coating. The surface temperature on the ceramic coating T_s varies from 1000^0C to 1600^0C. The substrate temperature remains invariable according to the actual application, i.e., $T_b = 700^0C$. When thermal cycle and the temperature on the surface the ceramic coating increase, the residual stresses at the interface are compressive and become higher and higher. As mentioned above, the accumulated compressive residual stresses may be up to a critical value and induce the buckling failure of the ceramic coating. The analysis in the next section will focus on the discussions of the buckling failure behavior of the ceramic coating under the effect of compressive residual stress and thermal cycles.

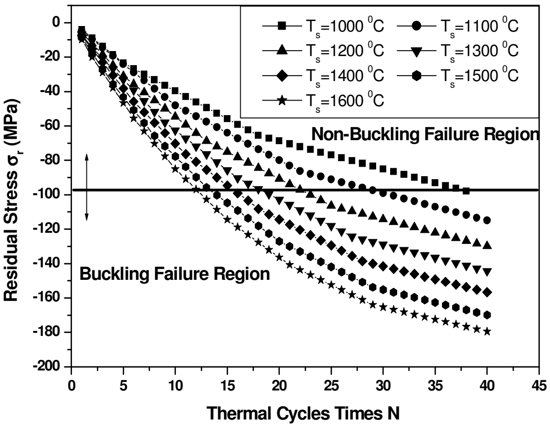

Fig.5 The relationship of residual stresses at ceramic coating/bond coat interface with thermal cycles, where the substrate temperature remains invariable, i.e. 700^0C.

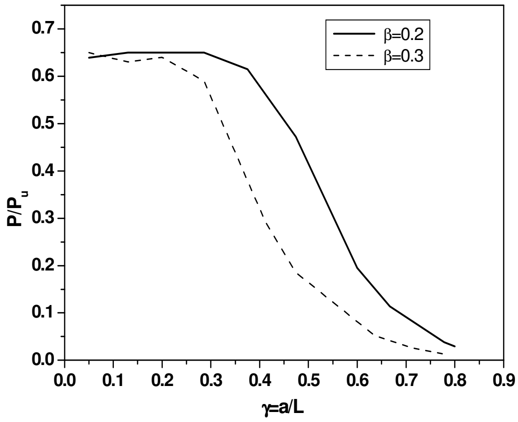

Fig.6 The relationship of the non-dimensional critical loading P/P_u with the non-dimensional crack length γ, where $\beta = h_c / H$.

Critical Buckling Stress. Generally, as we know, the critical buckling loading is mainly influenced by the interface cracking length a, the total thickness H, the total length L and the ceramic coating thickness h_c. The calculated results show that the interface crack length is the key parameter to control the critical buckling load. Fig.6 shows the relationship of non-dimensional critical buckling loading P/P_u with the non-dimensional interface crack length $\gamma = a/L$, where P_u denotes the critical buckling loading for the intact TBCs system. It can be seen that the dependence of the critical buckling load on the interface crack length is not very high when the crack is short. However, when the crack is long, for example, γ equals 0.3, the dependence of the critical buckling loading on the interface crack length is high. When the interface crack is very long, for example, γ equals 0.65, the critical buckling load is very low and the non-dimensional critical buckling load P/P_u is almost zero.

However, as studied by Choi et al. [14], the TBC system has sufficient stiffness to suppress small scale buckling (SSB) of the TGO. Accordingly, the eventual failure often occurs by large scale buckling (LSB) but only after a sufficiently large separation has developed at the interface, typically several mm in length. In this paper, the interface crack length is assumed to be $1mm$ and $0.1mm$. The corresponding critical bucking loads/stresses are, respectively, $-98.78MPa$ and $-1.2GPa$ by using the buckling failure model. It is obviously seen that the critical buckling stresses will be quickly decrease when the interface crack length increases during the thermal cycles. For interface delamination length $1mm$, the corresponding buckling stress is marked by bold line as shown in Fig 5. Therefore, when the residual stress in ceramic coating accumulates with thermal cycles and it is up to the corresponding critical buckling stress, the buckling failure phenomenon of the ceramic coating will occur. It is obviously seen that if the surface temperature T_s is low, the delaminated TBC system must experience more thermal cycles such that the residual stress accumulated in ceramic coating can be up to the buckling failure stress. When the surface temperature T_s becomes high, that is to say, the temperature gradient becomes large, the critical thermal cycles decrease rapidly. The accumulated residual stresses may be easy to achieve the critical stresses of the buckling failure of the ceramic coating. That is to say, when the temperature gradient along the thickness direction of TBCs increase, the buckling failure of the top coating in TBCs occurs easily.

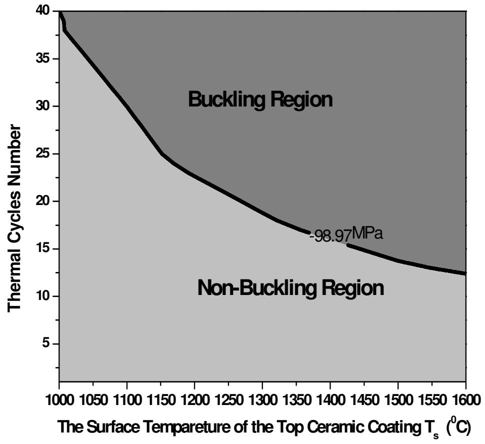

Fig.7. The buckling plane, i.e. $n-T_s$ is introduced to predict the buckling failure of the ceramic coating, where the interface length is 1.0mm

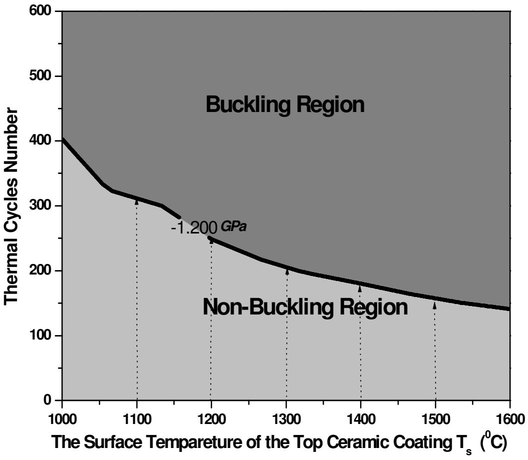

Fig. 8. The buckling plane is used to describe the relationship of residual stress, thermal cycles and temperature gradient, where the interface length is 0.1mm

In order to have a clearly physical information, the buckling plane, i.e. $n-T_s$ plane, is introduced to predict the buckling failure of the TBC system. Fig. 7 and Fig. 8 denote, respectively, two different kinds of the buckling plane for different interface crack length, i.e. $a=1mm$ and $a=0.1mm$. In the plane, there are two regions, i.e., non-buckling region and buckling region (top).

When T_s is 1000^0C and 1600^0C the critical thermal cycles are, respectively, 40 and 12 as shown in Fig.7. Comparing Fig.7 and Fig.8, it can be seen that the interface length and temperature gradient play an important role for the buckling failure of the ceramic coating.

Conclusions

The thermal residual stress and the critical buckling failure of ceramic coating have been studied. The following conclusions can be highlighted.

(1) An analytical solution of stress field in TBCs is obtained under the non-linear coupled effect of temperature gradient, thermal fatigue and creep strain of TBCs. The calculated results show that the residual stresses in ceramic coating are compressive. The accumulated residual stresses with thermal cycles could be high enough to induce the buckling failure of the ceramic coating. These conclusions are in good agreement with experimental phenomena.

(2) A theoretical model is proposed to predict the critical thermal buckling loads for the failure of TBC system. The important parameters for the critical buckling conditions are the interface crack length and the residual compressive stresses in ceramic coating. By calculation, it is found that when the interface crack is too short, the ceramic coating will not buckle. On the other hand, a buckling plane is introduced to predict the buckling failure of the ceramic coating. In the plane, it can be divided into two regions, i.e., non-buckling region and buckling region.

Acknowledgements

The project is sponsored by the Scientific Research Foundation for the Returned Overseas Chinese Scholars, State Education Ministry (No:[2002]247).

References

1. E. Celik, E. Avci, F. Yilmaz: Surf. Coatings Technol. Vol. 97 (1997), 361-365.
2. E. Celik, I. A. Sengil, E. Avci: Surf. Coatings Technol. Vol. 97 (1997), 355-360.
3. Y.C. Zhou, T. Hashida: Int. J. Solids Struct. Vol. 38 (2001), 4235-4264.
4. Y.C. Zhou, T. Hashida: JSME Int. J. Vol. 45 (2002), 57-64.
5. A.G. Evans, M.Y. He, J.W. Hutchinson: Progress Mater. Sci. Vol. 46 (2001), 249-271.
6. A.G. Evans, D.R. Mumm: Progress Mater. Sci. Vol. 46 (2001), 505-553.
7. A.M. Karlsson, C.G. Levi, A.G. Evans: Acta Mater. Vol. 50 (2002), 1263-1273.
8. R.J. Christensen,V.K. Tolpygo, D.R. Clarke: Acta Mater. Vol. 45 (1997), 1761-1766.
9. V. Sergo, G. Pezzotti: Acta Mater. Vol. 46(5) (1998), 1701-1710.
10. S.R. Choi, J.W. Hutchinson, A.G. Evans: Mech. Mater. Vol. 31 (1999), 431-447.
11. D.M. Zhu, A.M. Robert: J. Mater. Res., Vol. 14(1) (1999), 146-161.
12. C.C. Chiu, E.D. Case: Mater. Sci. Eng A., Vol. 132 (1999), 39-47.
13. D.K. Li, J.P. Zhou: Acta Mechanica Solida Sinica, Vol. 21(3), (2000), 225-233.
14. S.R. Choi, J.W. Hutchinson, A.G. Evans: Mech. Mater. Vol. 31 (1999), 431-447.